FIRST PRINCIPLES STUDY OF POROUS CARBON AS ANODE MATERIAL FOR METAL-ION (Na, Li, Mg) BATTERIES APPLICATIONS

AYUK CORLBERT AYUK

MASTER'S THESIS SUBMITTED TO THE DEPARTMENT OF MATERIALS SCIENCE AND ENGINEERING IN PARTIAL FULFILLMENT OF THE REQUIREMENTS FOR THE DEGREE OF MASTER OF SCIENCE

AT THE

AFRICAN UNIVERSITY OF SCIENCE AND TECHNOLOGY, ABUJA, NIGERIA

JUNE 2019.

Supervisor: Dr. Abdulhakeem Bello

FIRST PRINCIPLES STUDY OF POROUS CARBON AS ANODE MATERIAL FOR METAL-ION (Na, Li, Mg) BATTERIES APPLICATIONS By

AYUK CORLBERT AYUK

A THESIS APPROVED BY THE MATERIALS SCIENCE AND ENGINEERING DEPARTMENT

RECOMMENDED: ……....

Supervisor; Dr. Abdulhakeem Bello

…….....

Prof. Azikiwe Peter Onwualu

Head, Department of Materials Science and Engineering

APPROVED: …….....

Prof. Charles Chidume

Chief Academic Officer

…….....

Date

Certification

This is to certify that the thesis titled “First Principles Study of Porous Carbon as Anode Material for Metal-ion (Na, Li, Mg) Batteries Applications” submitted to the Department of Materials Science and Engineering, African University of Science and Technology (AUST), Abuja, Nigeria for the award of Master’s degree is a record of original research carried out by Ayuk Corlbert Ayuk.

Abstract

Sodium-ion batteries (SIBs) have been identified as an effective technology for grid-scale energy storage because of relatively low cost and natural abundance of sodium, but the lack of suitable anode materials with high Coulombic efficiency and reversible capacity has been a challenge. While graphite, an anode material in Lithium-ion batteries (LIBs), has been used for storing Na ions, its performance in terms of efficiency and capacity has been unsatisfactory for practical applications. Hard porous carbon has the promise to be an excellent anode in SIBs, but its atomic-scale structure is not known to pose a fundamental scientific question that must be addressed to understand the mechanism of its ability to store Na^+ ions. Here, we present a computational route to construct structural models of porous forms of carbon. Using first-principles density functional theory simulations we derive the model porous carbon structures of varying density (1.70, 1.85, 2.0 g/cm^3), and determine their interaction with intercalating Na, Li, and Mg atoms estimating the associated anodic voltages. While Li and Mg interact more strongly with porous carbon than Na ions, we demonstrate that carbon atoms are chemically more activated at a lower density of 1.7 g/cm^3 resulting in strong interaction with Na atoms and can be good anodic material in NIBs. Our comparative analysis of changes in the electronic structure of porous carbon with Na, Li, and Mg intercalation helps understand the mechanism of Na uptake into hard and porous carbon and will stimulate the development of improved carbon-based anodic materials for SIBs. All calculations were performed using the Quantum espresso simulation package, the total energy was calculated by the generalized gradient approximation coupled with PBE functional.

Keywords: Density Functional Theory; Sodium-ion batteries; Porous Carbon Model; Intercalation; Anodic material

Acknowledgment

I would like to express my sincere gratitude to my sponsor Pan-Africa materials institute (PAMI) for sponsoring my program and to Prof. Umesh Waghmare for the continuous support and scholarly inputs to my research. Despite his busy schedules, he has always made himself available to help me with my research. His sharp questions as well as effective comments in our discussions make me think deeply in my study and then understand the problems better. Many thanks are also given because of his kindness to me. Conferences that he offered me were precious experiences for me to train my presentation skill and to learn from other studies. I am deeply grateful to my supervisor Dr. Abdulhakeem Bello for his valuable guidance and consistent encouragement I received throughout my master's study and the research work. It is a treasured opportunity for me to be able to study from his specialized expertise. Working with him through 18 months of the Master course, I have also learnt from him his logically critical thinking and careful working manner. I must express my thankfulness to Professor Peter Azikiwe Onwualu, who had an important contribution to my Master's presentation through his course research methodology. I want to express my appreciation to all AUST faculties, who were very enthusiastic to help me with various courses during my master's study. I would also like to thank my group members and course mates who have provided me many interesting seminars and useful help. I am grateful to the Africa center of excellent (ACE) for Materials Science for the financial support granted through master fellowship. Finally, to whom I greatly indebted, thank you, mom, dad, and siblings for your unconditional support and throughout encouragement. What I have achieved today is thanks to you all.

Dedication

I dedicate this work to my family for the inspiration I get from them to study.

Table of Contents

List of Figures

CHAPTER ONE

1.0 INTRODUCTION

1.1 Background introduction

The importance of energy storage has grown to an unprecedented level in today's increasingly technologically driven, highly mobile, and energy-demanding society. The development of rechargeable battery technologies has been primarily influenced by the electronics industry, aerospace, military applications, and as energy sources for electric vehicles. While these applications for battery systems will remain, pressing needs regarding the efficient use of renewable energy resources to reduce fossil fuel consumption have contributed to battery research in recent years [2,3]. Increasing the use of renewable energy sources, such as wind and solar power, bring problems with modulating the resources over time and integrating them into the grid smoothly and safely. It is also important to balance electricity generation and demand between daytime and night-time to optimize grid utilization. Therefore, large-scale energy storage is extremely important to shift electrical energy from peak to off-peak periods. Among the various technologies proposed for renewable energy applications, secondary batteries appear to be one of the most promising means for storing electricity on a large scale because of its flexibility and high energy conversion [4,5]. Fossil fuel consumption of internal combustion engines gives rise to environmental pollution, that results in an urgent need for the development of hybrid electric vehicles (HEVs), plug-in hybrid electric vehicles (PHEVs) and electric vehicles (EVs). Research into secondary lithium-ion batteries is crucial in the development of these alternatives to petrol and diesel cars, as high energy and power density batteries are required [3, 6]. The limitation of lithium resources increased the cost of mining, and reliance on imports has made it necessary to explore alternative battery technologies. Sodium-ion batteries have gained interest in this regard as they offer similar chemistry to lithium-ion based systems since sodium behaves in a similar way

to lithium, and much more abundant metal and is, therefore, lower in cost. Although sodium-ion batteries are a promising alternative, they suffer two major issues when compared with their lithium counterparts. Firstly, Na has a lower ionization potential than Li, resulting in lower energy densities for sodium-ion batteries. Secondly, Na+ ions have a larger ionic radius and are heavier than Li^+ ions, which may lead to slower ion diffusion and large volume changes on the cycling of the electrode. Despite these factors, sodium-ion batteries would be an optimal choice for use in large-scale energy storage systems, where their lower gravimetric capacity is less important, as they could offer cells, which are low in cost and long life. The differences between lithium-ion and sodium-ion chemistries also mean that new crystalline solids can be explored to facilitate the intercalation/deintercalation process of the larger ions [3,4, 7-12].

Secondary batteries based on divalent ions, such as magnesium, are also under consideration as an alternative to Li-ion technologies. While the development of these cells is still in its infancy compared to Li-ion batteries, the prospects of increased energy density and the ability to use a metal anode make magnesium batteries promising for future commercial use. However, several challenges need to be overcome before this is a possibility, including the development of a suitable cathode and anode material as Mg^{2+}, suffer from slow diffusion through more conventional insertion compounds [13-16]. This introduction chapter will first outline the components and materials in lithium-ion batteries, followed by details of sodium-ion and magnesium materials for batteries, including the compounds examined in this work.

1.2 Batteries for Electrochemical storage

A battery is a device that converts the chemical energy contained in its active materials directly into electric energy through an electrochemical oxidation-reduction (redox) reaction. Batteries can be classified into two categories: primary batteries, which use the chemicals once only in a single discharge, and secondary batteries or "rechargeable batteries", which can be recharged by a reversal of the process and reused again. While the term ''battery'' is often used, the basic electrochemical unit is the ''cell.'' A battery consists of one or more of these cells, connected in series or parallel, or both, depending on the desired output voltage and capacity. The cell consists of three major components: anode, cathode, and electrolyte (Fig 1.1).

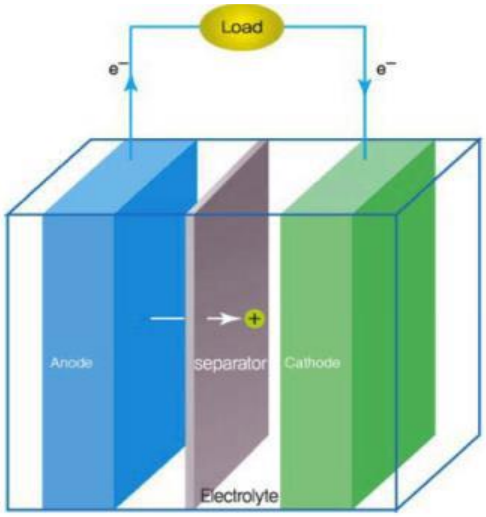

Fig 1. 1 Scheme of an electrochemical cell during discharge Source: Wikipedia

During the discharge of batteries, the process of converting chemical energy carried by the battery into electric energy takes place while electrochemical oxidation of the electrode (A→A+e-) proceeds at the anode. Electrons transferred from the negative terminal through the external circuit engage in reduction (B++e-→B) at the positive terminal, which is known as a cathode. The electrolyte serves as an ionic conductor of the ions between the two electrodes guaranteeing the electro-neutrality. It is typically an organic solvent with dissolved salts to impart ionic conductivity

although they can be also ceramic, polymeric, or composite. The cell voltage depends on the potential difference between the two electrodes [11,12].

The amount of electrical specific energy, ($W \cdot h\ kg^{-1}$) or volumetric energy ($W \cdot h \cdot l^{-1}$), that a battery can deliver is a function of the cell potential (V) and capacity ($A \cdot h \cdot kg^{-1}$), both of which are related to the chemistry of the system. In Fig 1.2 some of the various existing technologies in the market for EES are compared as a function of the volumetric and gravimetric energy densities. The main characteristics and technical properties of different technologies are summarized in Table 1.1.

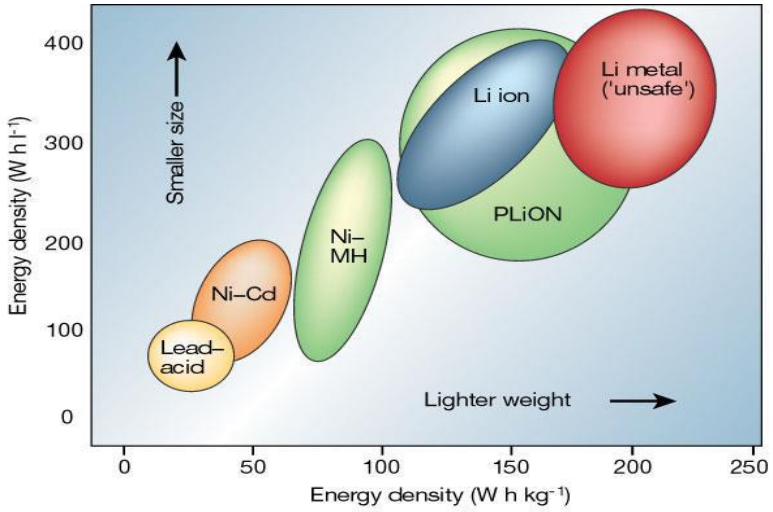

Fig 1. 2 Comparison of the volumetric and gravimetric energy densities of different rechargeable batteries for EES [13].

Lead-acid batteries have fast response times, small daily self-discharge rates, and relatively high cycle efficiencies (63-90%). However, they have limited energy density, risk of hydrogen evolution, and require the use of heavy metals. Although the cost of a lead-acid battery is relatively low, it is not a good option for large-scale EES applications due to its relatively short lifetime. Typical applications of lead-acid batteries include automotive power (starting the engine, electric and hybrid vehicles) and standby emergency power. Although they show higher reliability in terms of specific energy, cycle life, and round-trip efficiency of Pb-acid batteries, to date there have been

very few commercial successes using **Ni-Cd batteries** for EES applications. The weaknesses of this technology are the use of toxic heavy metals and memory effects. They are mainly used for railroad and mass-transit installations aircraft batteries, lighting, emergency power, and power stations. The metal hydride electrode of **Ni metal hydride batteries** (Ni-MH) has a higher energy density than the cadmium electrode resulting in a higher capacity or longer service life. In the portable sealed configuration, it is being used in consumer electronic devices (cellular phones, transceivers, computers, etc).

Sodium-sulfur battery (Na/S) technology is commercially available for grid applications, with some 200 installations worldwide, accounting for 315 MW of discharge power capacity. However, the main drawback is to maintain operating temperatures a heat source is required, which uses the battery's stored energy, partially reducing the battery performance [14]. Redox flow batteries like **vanadium redox battery** (VRB) are especially advantageous because the power is independent of its storage capacity. It is determined by the size of the electrodes and the number of cells in the stack; whereas the storage capacity is determined by the concentration and the amount of electrolyte. They show very small self-discharge but they also show low performance resulting from non-uniform pressure drops and the reactant mass transfer limitation, relatively high manufacturing costs, and more complicated system requirements compared to traditional batteries [8]. There are not many commercially available redox flows battery systems at present. **Lithium-ion batteries** (Li-Co and Li-FP) offer superior energy efficiency, high power density, fast charge, and discharge capability, low weight, and long cycle life. The main disadvantages are the high cost due to overcharging protection circuitry and the risk of capacity loss or thermal runaway. Given their high energy density, they are suitable for portable applications (electronics, vehicles). That explains the share of worldwide sales for Li-ion portable batteries (63%) is much larger than those

for Ni-Cd (23%), Ni–MeH (14%) [13].

1.2.1 Li-ion batteries

The first commercial Li-ion battery (LIB) was developed by Sony in the 90s and contained $LiCoO_2$ and petroleum coke as cathode and anode, respectively [18]. Li-ion batteries quickly became a competitive technology for portable devices thanks to their high energy and power density. In most commercial lithium-ion batteries, active materials undergo a topotactic reaction where lithium ions are reversibly removed or inserted into a host, without a significant structural change to the host. They are also referred to as rocking-chair batteries as the lithium ions ‘‘rock’’ back and forth between the positive and negative electrodes as the cell is charged and discharged.19 However, there are also alloying and conversion processes. In the latter, the material undergoes a solid-state redox reaction during lithiation/delithiation, in which changes in the crystalline structure, accompanied by the breaking and recombining chemical bonds have been extensively studied. The reaction mechanisms is illustrated in Fig 1.3

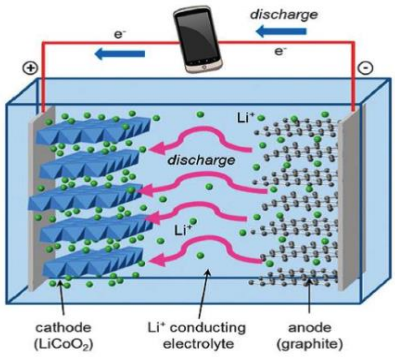

Fig 1. 3 Schematic of a typical rechargeable lithium-ion battery with a $LiCoO_2$ cathode and graphite anode. During charging, Li+ ions flow to the anode through electrolyte and electrons travel through the external circuit [18].

1.2.2 Sodium-ion batteries

Lithium-ion has been successfully employed as a charge carrier for secondary batteries due to its good performance derived from their small ionic size allowing fast kinetics and low atomic number leading to high theoretical specific capacity and energy density. These characteristics have made lithium-ion batteries to be fully integrated into portable devices and electric vehicles. However, there is much controversy about the extent of lithium´s reserves29. The large scale demand for this alkali might increase its price shortly due to the low abundance of it on the Earth´s crust.5 This global situation has driven researchers to investigate new battery technologies based on abundant resources such as magnesium-sulfur, sodium ion, and magnesium ion batteries [30,31,32]. Sodium-ion batteries were investigated in parallel to the lithium-ion batteries during the 80s [33]. However, lithium-ion batteries drew attention due to their higher energy density. Despite Na chemical similarity to Li, there are significant differences between them as presented in Table 1.2.

Table 1.1 Comparison of the characteristics of Na and Li [34,5].

CHARACTERISTICS	Na	Li
Cation radius	1.02 Å	0.76 Å
Atomic weight	23 $gmol^{-}$	6.9 $gmol^{-1}$
E_0 VS. SHE	-2.7 V	-3.04 V
Melting Point	97.7 °C	180.5 °C
Abundance	$23.6.10^3$ $mgkg^{-1}$	20 $mg.kg^{-1}$
Distribution	Everywhere	70 % in South America
Price, Carbonates	0.07 -0.37 €.kg^{-1}	4.11 – 4. 49€.kg^{-1}

Na is cheaper, more abundant and it is more evenly distributed than Li, which is mostly located in South America, and, the production of LIB depends on the import of Li. Moreover, it is possible to use Al current collectors in the anode electrode instead of Cu, as happens for Li batteries, which can be translated into a decrease in the cost of the battery. However, despite Na and Li are chemically similar, the larger size of Na ions results not only in lower volumetric capacity compared to lithium but also in the lithium-ion technology being non-fully transferable to sodium. On the one hand, the different size between Li and Na affects the properties in the host structure of the intercalated and deintercalated materials and, on the other hand, the existence of different surface passivation processes can lead to different electrochemical performance. Direct anodic application of elemental alkali metals (lithium or sodium) in rechargeable alkaline ion batteries causes poor cycle performance and short-circuits because of their low melting point (180.5 ºC for Li and 97.7 ºC for Na), high chemical reactivity and dendritic growth during charge and discharge.

Therefore, the major challenge in developing sodium-ion technology lies in finding good electrode materials [35]. An obvious place to look for good Na electrode materials is by starting at structures and chemistries that work well for Li intercalation. This is because the open crystal structure that allows Li intercalation is often suitable for Na intercalation. Regarding the applications, sodium-ion batteries are becoming one of the most promising alternative technologies for stationary energy storage because the weight of the device is not of primary importance, while the higher energy density makes lithium more appropriate for portable applications. For stationary applications, long cycle life, low cost, and high safety are the most important parameters. Hence, abundant, non-toxic, stable, and low-strain electrode materials need to be developed to ensure large-scale and long-term applications and to decrease battery management costs.

Recent developments in cathode materials for sodium-ion batteries include layered oxides, polyanions, Prussian blue, and organic compounds. Anode materials can be categorized into carbonaceous materials, transition metal oxides, or sulfides, metal alloys, and organic compounds. In the next section, a short description of the main electrode materials reported for sodium-ion batteries will be summarized.

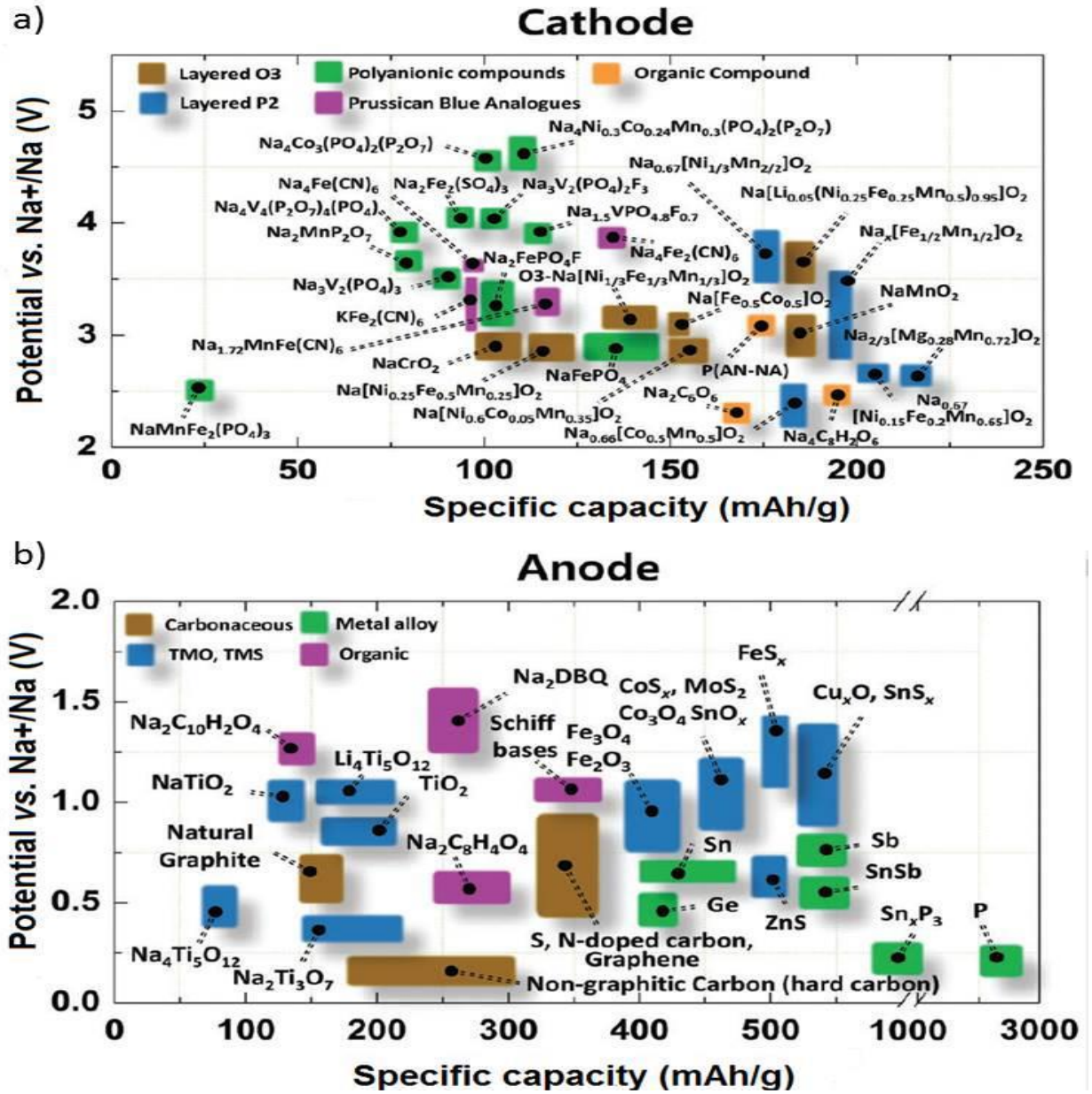

Fig 1. 4 Recent research progress in materials for sodium-ion batteries: (a) cathode, (b) anode

Source: www.google.com

1.2.3 Magnesium ion battery

As mentioned above the challenges facing lithium-ion batteries have increased research interest in post-lithium technologies. Rechargeable magnesium batteries presents a promising technology for energy storage. Magnesium-based technology is promising for several reasons. Firstly, Mg is abundant in the Earth's crust than Li, making it a cheaper metal to incorporate into electrode materials. Secondly, Mg is more atmospherically stable than Li and has a higher melting point, this makes it safer to handle and manufacture. The divalent nature of the Mg ion means it is also able to offer a potential advantage in terms of energy density [13–16]. One of the huge challenges facing Mg batteries is the development of a suitable electrolyte that is capable of reversible metal plating/stripping at the anode and supporting reversible intercalation against a high voltage cathode. A multitude of factors has slowed the development of a functional magnesium electrolyte, including limited electrochemical stability with the electrodes (i.e. narrow electrochemical stability window), lack of reversible Mg metal stripping and plating, instability against current collectors and low Mg mobility, leading to the formation of ionic couples.

1.3 Carbon anode for metal-ion batteries.

1.3.1 Carbon materials

There are several carbon allotropes, for example, graphite with a sp2 hybrid orbital, a diamond with a sp3 hybrid orbital, and carbine with an sp hybrid orbital. Among them, sp2 carbons have been extensively studied as electrode material candidates for Lithium, sodium rocking chair batteries because they are capable of undergoing reversible intercalation/deintercalation of sodium.

1.3.1.1 Structure of sp^2 carbons

Graphite.

In graphite, graphene layers are formed by carbon atoms of the sp2 hybrid orbital layered along a hexagonal plane. Delocalized π electrons have Van der Waals bonding between graphene layers. Since π electrons have the freedom to move between graphene layers, graphite has good electronic conductivity.1 In naturally occurring or high-quality graphite, the stacking sequence of the layers is generally ABAB with an interlayer 002 spacing of approximately 0.334 nm. (Figure 1.5)

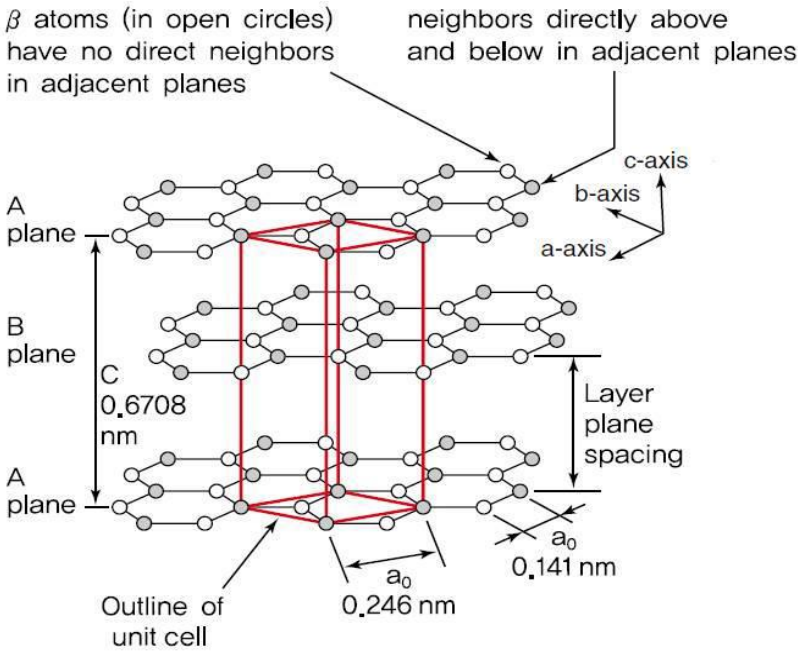

Fig 1. 5 Hexagonal unit cell of graphite. Source: www.google.com

Disordered carbons.

Most real materials contain disorder, including the 2H (hexagonal unit cell, ABABAB) and 3R (rhombohedral unit cell, ABCABC) stacking orders as well as random stacking [2]. Disordered or non-graphitic carbons exhibit a structure in which most of the carbon atoms are also arranged in a planar hexagonal network but long-range ordering in the c direction is lacking [3]. This structure is characterized by amorphous areas embedding and partially crosslinking (by sp3 hybridized

carbon atoms) more graphitic layered structure segments consisting of aligned small-dimensionality sp2 graphene layers. Stacking disorders include those where the graphitic planes are parallel but shifted or rotated, termed turbostratic disorder. Disordered carbons that maintain a compact lamellar fine structure are mechanically soft like graphite. These disordered carbons are named "soft" or graphitizable carbons because they can be graphitized under heat treatment. In general, the graphitization process includes the expansion and stacking of graphitic planes, in a three-dimensional manner. During graphitization, carbon undergoes an increase in density and crystallite sizes (La and Lc), respectively, and a decrease in (002) interplanar spacing. (Figure 1.6) The turbostratic disorder is removed and strain in the material, relieved. In soft carbons, the crosslinking between the layers is weak due to Van der Waals bonding, so layers are mobile enough upon further heat-treatment at high temperatures to form graphite-like crystallites. In contrast, strong cross-linking will immobilize graphene layers avoiding graphitization by heat treatment and increasing their mechanical strength leading to "hard" or non-graphitizable carbons. The final product after pyrolysis will be hard or soft carbon depends mainly on the nature of the precursor. Oxygen-rich precursors tend to form hard carbon whereas hydrogen-rich precursors usually lead to soft-carbons. Soft carbons are usually obtained from highly condensed aromatic hydrocarbon precursors such as mesophase pitch [20], coal tar pitch [21], phosphorous doped pitch [22 3,4,9,10] perylene-tetracarboxylic acid-dianhydride (PTCDA) [23] or from petroleum or coal refinement or plastics with low oxygen content.

1.3.1.2 Sodium storage mechanism of sp2 carbons

Graphite. Graphite is the most common anode material for commercialized LIBs, which exhibit a capacity of 372 $mA{\cdot}h{\cdot}g^{-1}$, corresponding to the formation of graphite intercalation compound

(LiC_6) [24]. However, the conventional graphite cannot be applied as efficient anode material for SIBs in the usual way since the sodium intercalation into graphite is limited to the formation of NaC70 equivalent to poor capacity of 31 $mA \cdot h \cdot g^{-1}$ [25]. To realize the sodium storage of graphite special treatments have to be undertaken. One approach is based on the use of graphite oxide and expanded graphite, due to the enlargement of the interlayer spacing, can effectively store Na+ through intercalation [26]. However, intercalation is not just a matter of diameter of the intercalating alkali metal as the insertion through the co-intercalation of Na^+ and solvent molecules has been reported to happen according to the reaction in Eq. 2.1.

Disordered carbons. Due to their good conductivity, non-toxicity, electrochemical activity at low voltages, and potentially low cost, disordered hard and soft carbons are the main candidates to become anode materials in commercial sodium-ion batteries. The nature of the reaction mechanism of sodium insertion in disordered carbons is controversial. The existing proposed mechanisms are summarized below.

Insertion-Adsorption mechanism

Until recently, it has been accepted the "house of cards" (Figure 1.6 a) mechanism proposed by Dahn et al. in 2000 is valid. According to Dahn et. al, in disordered carbons, the turbostratic disorder between graphene layers creates interlayer insertion sites for sodium ions within a range of chemical environments, giving rise to a range of potentials. The sloping voltage on the electrochemical profile below 1 V vs. Na+/Na. Additionally, hard carbons show a low voltage plateau which is ascribed to the filling of the micro-pores of the voids between randomly stacked layers.

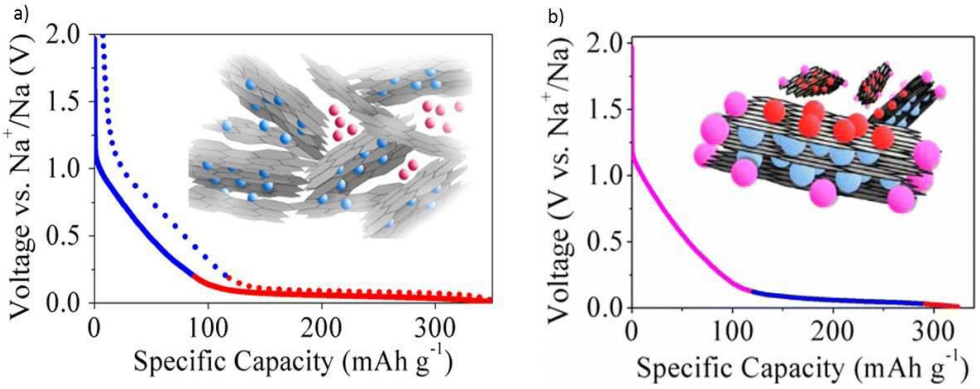

Fig 1. 6 Visual representation of a) the house of cards model for the sodium/lithium storage in hard carbon showing two distinct parts in the voltage profile: intercalation inside the turbostratic nanodomains (blue) and pore-filling (red). b) The three-step mechanism proposed by Bommier et al. showing three distinct binding sites [31].

Although some experimental results have confirmed this mechanism, researchers have also found that it cannot be used to explain several experimental phenomena. For the same precursor, there are lots of micropores in the hard carbon pyrolyzed in low temperature, but low plateau capacity is exhibited. Besides the micropore volume of carbon decreases with the increase of pyrolytic temperature, the plateau capacity gradually increases [30].

Adsorption- Insertion mechanism.

Bommier *et al.* found that the slope capacity plotted against defect concentration lead to a linear relationship evidencing that defected carbon sites are responsible for the slope capacity rather than turbostratic nanodomains. These defects (monovacancies, stone-wales defects, extreme curvature in graphene sheets, and the presence of sp^3 linking carbons that connect neighboring turbostratic nanodomains, etc) might have its sodiation voltage leading to a sloping voltage. They also observed expansion and contraction of d-spacing at the plateau region suggesting that intercalation

occurs at low voltages. Based on these results above, it was concluded that the slope region is related to the sodium storage on edges and surface defects of carbon, rather than micropores, and the low potential plateau region corresponds to the insertion of Na^+ into carbon interlayers and minor Na^+ adsorption on pore surfaces (Figure 2.3b). The mechanism proposed by Dahn *et al.* was supported by the experiments showing that the interlayer distance varies during the sloping region [32]. Ex-situ nuclear magnetic resonance (NMR) performed on hard carbons also demonstrated that low voltage plateau is related to sodium insertion of sodium ions forming quasi-metallic clusters in closed nanopores of hard carbon [33]. The existence of a contradiction between results might be indicative of both mechanisms taking place at the same time. Further studies would be required to fully understand these mechanisms [6].

1.3.1.3 Electrochemical performance of sp^2 carbons

Graphite: Prepared through a process of oxidation and partial reduction on graphite, expanded graphite has an enlarged interlayer lattice distance of 4.3 Å yet retains an analogous long-range-ordered layered structure to graphite and provides capacities close to 290 $mA{\cdot}h{\cdot}g^{-1}$ [26]. When the diglyme was used as the solvent with commercial graphite leads to an intercalation compound with an estimated stoichiometry of Na(diglyme)2C20, a reversible capacity of 100 $mA{\cdot}h{\cdot}g^{-1}$ was delivered with excellent capacity retention for 1000 cycles [27]

The use of graphite as anode for sodium-ion batteries, however, still entails some problems. Firstly, the intercalation of solvent molecules would lead to the consumption of electrolyte solvent, inducing the increase of resistance and demand for the excess electrolyte. Secondly, the low specific capacity and high intercalation voltage would cause a decrease in energy density in the full battery system [30]. Additionally, the large volume expansion (≈350 %) originating from the

co-intercalation behavior would result in the pulverization of graphite particles in the repeated charge-discharge cycles, leading to the degradation of cycling performance [34].

Disordered carbons: A variety of amorphous carbon materials, have been employed as anode materials for SIBs with several micro/nanostructures. Due to fact that their kinetics are favorable for the transportation of ion and electron, some structures such as hollow nanostructured hard carbon materials [35], nano cellular carbon foams [36], templated carbon, carbon microspheres, hierarchically porous carbon/graphene composite materials, carbon nanofibers, carbon nanotubes, carbon nanoparticles, and carbon nanosheets have been evaluated as anode materials. The introduction of heteroatoms (*e.g.*, B, N, S, and P) has been considered as a quite promising approach to enhance the capacity, surface wettability, and electronic conductivity, which can promote the charge transfer and electrode/electrolyte interactions. Thus, a variety of heteroatom-doped carbonaceous materials with several morphologies has been widely explored as anode materials for SIB. For example, N-doped bamboo-like carbon nanotubes produced from pyrolysis of a mixture of dicyandiamide (DCD) and $CoCl_2$ can deliver 270 $mA \cdot h \cdot g^{-1}$ at 50 $mA \cdot g^{-1}$ and good rate capability attributed to short Na^+ diffusion distance and a large electrode/electrolyte contact [44]. Likewise, N-doped carbon nanofibers obtained by pyrolysis of polypyrrole, deliver 172 $mA \cdot h \cdot g^{-1}$ of reversible capacity [40]. However, the low initial Coulombic efficiency (~30-40 %) of this type of nanostructured materials is the main limiting factor for real applications.

Soft carbons: Sodium can be reversibly inserted into amorphous and non-porous carbon black, a highly pure elemental carbon in the form of colloidal particles that are produced by incomplete combustion or thermal decomposition of gaseous or liquid hydrocarbons. Carbon black provides a reversible capacity ~ 200 $mA \cdot h \cdot g^{-1}$. However, a large irreversible capacity arising from the high surface area is observed [45]. Other soft carbons such as mesoporous carbon derived from

mesophase pitch or cellulose deliver reversible capacities as high as 331 $mA \cdot h \cdot g^{-1}$ (0.08 C) and 375 $mA \cdot h \cdot g^{-1}$ (0.05 C), respectively. Pyrolysis of coal tar pitch also provides soft carbons with increased layer spacing and defects thanks to phosphorus doping which leads to good electrochemical performance (251 $mA \cdot h \cdot g^{-1}$ at 0.27 C) [22]. Apart from the mentioned contents, many soft carbon materials have been studied as anode materials for sodium-ion batteries.

***Hard carbons*.** One of the most employed anodes for NIBs is hard carbon whose electrochemical performance depends on the synthesis conditions such as carbon source and carbonization temperature. First, hard carbons as anodes of sodium-ion batteries were reported in 2000 by Stevens and Dahn, who obtained a high reversible capacity of 300 $mA \cdot h \cdot g^{-1}$ by carbonization of glucose at 1000 °C. Presently, there exist commercially available pitch derived hard carbons (Carbotron P of Kureha Corporation). It delivers a reversible capacity of 200 $mA \cdot h \cdot g^{-1}$ corresponding to a stoichiometry of NaC11 with a first cycle Coulombic efficiency of 69 % (at C/25) [47]. The regulation of nanoparticle morphology and the introduction of nano porosity are common strategies to accomplish highly reversible Na^+ storage via artificially tailored nanopores. For example, a sugar derived nanoporous hard carbon provides 324 $mA \cdot h \cdot g^{-1}$ of reversible capacity with 76 % of initial Coulombic efficiency [48]. Compared to bulk sugar derived hard carbon, these nanostructured materials show, as usual, slightly improved capacity at high cycling rates but similar reversible capacities compared with pristine hard carbon at low rates [14]. The pyrolysis of polymers such as polyvinyl chloride (PVC) or polyvinylpyrrolidone (PVP) or resins like resorcinol-formaldehyde (R-F) leads to hard carbons. The use of PVC nanofibers as hard carbon precursor leads to 256 $mA \cdot h \cdot g^{-1}$ of reversible capacity with 66 % of the first cycle Coulombic efficiency and retention of 215 $mA \cdot h \cdot g^{-1}$ after 120 cycles at 0.03 C.49. The former provides better reversible capacity (271 $mA \cdot h \cdot g^{-1}$ at 0.05 C) but lower first cycle irreversible

capacity (48 %) [7], the pyrolysis of R-F leads to the attainment of binder-free monoliths with a macroporous structure that provides large capacities close to 350 $mA \cdot h \cdot g^{-1}$ at C/20 with high first cycle Coulombic efficiency (92 %) [11]. Many hard carbons have been reported through pyrolysis of biomass precursors, which are renewable, abundant, and eco-friendly. The wide range of biomass precursors having different microstructures and chemical compositions that can directly determine the structure/morphology of the derived carbon materials opens infinite possibilities to the synthesis of hard carbons with different properties. Besides, the biomass materials often contain some heteroatoms (*e.g.*, O, N, S, and P), thus the derived carbon materials doped with these heteroatoms can be directly obtained by carbonizing treatment. The use of non-edible wastes as carbon precursors such as pomelo peels, corn cobs, peanut shells, etc. [30] have become interesting. For instance, shaddock peels, which have highly cross-linked and non-crystalline hemicellulose can form non-graphitic carbon that delivers up to 430 $mA \cdot h \cdot g^{-1}$ of reversible capacity (at 30 $mA \cdot g^{-1}$) with 69 % of the first cycle Coulombic efficiency and good rate performance [50]. Peanut shells that are lignin-based, also have a cross-linked structure can be transformed into hard carbons delivering a capacity of 298 $mA \cdot h \cdot g^{-1}$ with high capacity retention (98% after 300 cycles at a low current rate of 0.1 C) [51].

CHAPTER TWO

2.0 First-Principles Calculations

All the results in this thesis were based upon the first-principles calculations. The first principles method or *Ab initio* is a method that requires only basic properties such as atomic radius, number of electrons, nuclear-charge density, and so on as inputs. These initial inputs together with fundamental scientific rules can produce the true state of a physical system without the assistance of any empirically adjustable parameter. In this Chapter, two kinds of the first principles calculations; the density functional theory (DFT) and the hybrid functional methods, will be presented in Section 1 and 2. The last section is dedicated to the nudged elastic band (NEB) method for calculations of the activation energy.

2.1 Density Functional Theory

One of the main computational tools employed in this thesis is DFT. In DFT, the ground state energies of atomic systems are computed from the electron density. Throughout this thesis, DFT will be used to compute the lowest energy structures in various systems. The lowest energy structures of materials are typically the most interesting from a scientific point of view since they are the most likely configurations in which to find a system. In this section, the theoretical basis for DFT is presented. In principle, to compute the energy of a collection of atoms, one would solve the Schrodinger equation (shown below in its time-independent form): density functional theory is the theory, in which properties of many-body systems can be determined by using the functionals depending on electron density. The DFT has its origin from Hohenberg-Kohn theorem [28] which states that: the external potential $V_{ext}(\vec{r})$ is (to within a constant) a unique functional of $\rho(\vec{r})$; since, in turn $V_{ext}(\vec{r})$ fixes $\widehat{H}$ we see that the full many particle ground state is a unique functional

of ρ($\vec{r}$). $F_{HK}[\rho]$, the functional that delivers the ground state energy of the system, delivers the lowest energy if and only if the input density is the true ground state density.

2.1.1 Kohn-Sham equations

The time-independent, non-relativistic Schrödinger equation of a physical system consisting of M nuclei and N electrons is:

$$\widehat{H}\Psi_i(\boldsymbol{x_1}, \boldsymbol{x_2}, \dots, \boldsymbol{x_N}, \boldsymbol{R_1}, \boldsymbol{R_2}, \boldsymbol{R_M}) = E_i\Psi_i(\boldsymbol{x_1}, \boldsymbol{x_2}, \dots, \boldsymbol{x_N}, \boldsymbol{R_1}, \boldsymbol{R_2}, \boldsymbol{R_M}), \quad (1)$$

where the Hamiltonian $\widehat{H}$ is defined as

$$\widehat{H} = -\frac{1}{2}\sum_{i=1}^{N}\nabla_i^2 - \frac{1}{2}\sum_{A=1}^{M}\frac{1}{M_A}\nabla_A^2 - \sum_{i=1}^{N}\sum_{A=1}^{M}\frac{Z_A}{r_{iA}} + \sum_{i=1}^{N}\sum_{j>i}^{N}\frac{1}{r_{ij}} + \sum_{A=1}^{M}\sum_{B>A}^{M}\frac{Z_A Z_B}{R_{AB}}. \quad (2)$$

The first two terms are the kinetic energy of the electrons and nuclei. The next term represents the attractive electrostatic potential between the nuclei and the electrons. The last two terms express the repulsive potential produced by the interactions between electrons-electrons and nuclei-nuclei. Because the nuclei are much more massive than the electrons, their kinetic energy can be approximated to be zero and their potential can be considered as a constant. Hence, we only need to pay attention to the electronic Hamiltonian:

$$\widehat{H}_{elec} = -\frac{1}{2}\sum_{i=1}^{N}\nabla_i^2 - \sum_{i=1}^{N}\sum_{A=1}^{M}\frac{Z_A}{r_{iA}} + \sum_{i=1}^{N}\sum_{j>i}^{N}\frac{1}{r_{ij}} = \hat{T} + V_{Ne} + V_{ee} \quad (3)$$

According to the Hohenberg-Kohn theorem, three above terms all depends on the electronic density ρ($\vec{r}$), thus the electronic energy becomes

$$E[\rho] = E_{Ne}[\rho] + T[\rho] + E_{ee}[\rho] \quad (4)$$

Explicit forms of these three terms can be expressed as follows

$$E_{Ne}[\rho] = \int \rho(\boldsymbol{r})\, V_{Ne}(\boldsymbol{r}) d\boldsymbol{r}, \tag{5}$$

$$E_{ee}[\rho] = E_{Hartree}[\rho] + E_{ncl}[\rho] = \frac{1}{2}\int\int \frac{\rho(\boldsymbol{r_1})\rho(\boldsymbol{r_2})}{r_{12}} d\boldsymbol{r_1} d\boldsymbol{r_2} + E_{ncl}[\rho] \tag{6}$$

where $E_{\text{ncl}}[\rho]$ is the non-classical contribution as self-interaction correction, exchange and Coulomb correlation. The kinetic component can be calculated as the sum of the kinetic energy of a non-interacting system with an unknown part. This unknown part will be computed later by some approximations.

$$T[\rho] = T_n[\rho] + T_u[\rho] = -\frac{1}{2}\sum_i^N \langle \Psi_i |\, \nabla^2 |\, \Psi_i \rangle + T_u[\rho]. \tag{7}$$

Finally, the electronic energy has the following form:

$$E[\rho] = \int \rho(\boldsymbol{r})\, V_{Ne}(\boldsymbol{r}) d\boldsymbol{r} + \frac{1}{2}\int\int \frac{\rho(\boldsymbol{r_1})\rho(\boldsymbol{r_2})}{r_{12}} d\boldsymbol{r_1} d\boldsymbol{r_2} - \frac{1}{2}\sum_i^N \langle \Psi_i |\, \nabla^2 |\, \Psi_i \rangle + E_{XC}[\rho], \tag{8}$$

in which the exchange-correlation function, $E_{XC}[\rho] = E_{ncl}[\rho] + T_u[\rho]$, is the only unclear part that needs further investigation.

After applying the variational principle, the obtained equations are the Kohn-Sham equations:

$$\left(-\frac{1}{2}\nabla^2 + \left[\int \frac{\rho(\boldsymbol{r_2})}{r_{12}} + V_{XC}(\boldsymbol{r_1}) - \sum_A^M \frac{Z_A}{r_{1A}}\right]\right)\Psi_i = \left(-\frac{1}{2}\nabla^2 + V_s(\boldsymbol{r_1})\right)\Psi_i = \epsilon_i \Psi_i \tag{9}$$

$$V_s(\boldsymbol{r_1}) = \int \frac{\rho(\boldsymbol{r_2})}{r_{12}} + V_{XC}(\boldsymbol{r_1}) - \sum_A^M \frac{Z_A}{r_{1A}}. \tag{10}$$

2.2 Exchange-correlation functions

2.2.1 The local density approximation (LDA)

The idea of local density approximation [29,30] is that electrons in a solid behave like a uniform gas. In this model, the exchange-correlation energy density, $\varepsilon_{XC}\big(\rho(\boldsymbol{r})\big)$, at each point is assumed to be the same as in a homogeneous electron gas. For spin-unpolarized system, the exchange-correlation energy has the following form:

$$E_{XC}^{LDA}[\rho] = \int \rho(\boldsymbol{r})\varepsilon_{XC}\big(\rho(\boldsymbol{r})\big)d\boldsymbol{r} \tag{11}$$

The quantity $\varepsilon_{XC}\big(\rho(\boldsymbol{r})\big)$ can be split further into exchange and correlation contributions,

$$\varepsilon_{XC}\big(\rho(\boldsymbol{r})\big) = \varepsilon_X\big(\rho(\boldsymbol{r})\big) + \varepsilon_C\big(\rho(\boldsymbol{r})\big). \tag{12}$$

The exchange part of the uniform electron gas, $\varepsilon_X\big(\rho(\vec{\boldsymbol{r}})\big)$, was derived by Bloch and Dirac as

$$\epsilon_X = -\frac{3}{4}\left(\frac{3\rho(\boldsymbol{r})}{\pi}\right)^{\frac{1}{3}}. \tag{13}$$

The correlation energy density can be obtained by highly accurate numerical quantum Monte-Carlo simulations [31]. For the spin-polarized system, the total exchange-correlation energy can be written as,

$$E_{XC}^{LDA}[\rho_\uparrow, \rho_\downarrow] = \int \rho_\uparrow(\boldsymbol{r})\varepsilon_{XC}\big(\rho_\uparrow(\boldsymbol{r})\big) + \rho_\downarrow(\boldsymbol{r})\varepsilon_{XC}\big(\rho_\downarrow(\boldsymbol{r})\big)d\boldsymbol{r}. \tag{14}$$

The exchange part is known in terms of the spin-unpolarized functionals:

$$E_X[\rho_\uparrow, \rho_\downarrow] = \frac{1}{2}\big(E_X(2\rho_\uparrow) + E_X(2\rho_\downarrow)\big), \tag{15}$$

in which $\rho\uparrow$, $\rho\downarrow$ denote for the up-spin and down-spin densities, respectively. The spin-dependent correlation energy is a function of two variants: the electronic density and the relative spin-polarization as well,

$$\zeta = \frac{\rho_\uparrow - \rho_\downarrow}{\rho_\uparrow + \rho_\downarrow}. \quad (16)$$

The correlation energy $E_C[\rho, \zeta]$ is constructed to interpolate extreme values $\zeta = 0, \pm 1$.

Because the non-homogeneity of electronic density is ignored, the LDA method gives many errors, such as underestimating the atomic ground-state energy, overestimating the binding energy, and wrongly predicting the energy gap of semiconductors.

2.2.2 The generalized gradient approximation (GGA)

The improvement of GGA compared to LDA is the addition of the gradient of the charge density, $\nabla\rho(\vec{r})$ to explain for the non-homogeneous electron gas in the real solid. One of the most widely used GGAs is in the form proposed by Perdew, Burke, and Enerhof [32] (PBE) which was used in the calculation of amorphous carbon models system; hence, only the PBE functional is presented in this Section. The exchange-correlation energy can be written as

$$E_{XC}^{GGA}[\rho_\uparrow, \rho_\downarrow] = \int f\left(\rho_\uparrow, \rho_\downarrow, \nabla_{\rho_\uparrow}, \nabla_{\rho_\downarrow}\right) d\vec{r}. \quad (17)$$

The explicit form for correlation energy is [33]

$$E_C^{GGA}[\rho_\uparrow, \rho_\downarrow] = \int \rho[\varepsilon_C^{LDA}(r_s, \zeta) + H(r_s, \zeta, t)]d\vec{r}, \quad (18)$$

where rs is the local Seitz radius $\rho = \frac{3}{4\pi r_s^3} = \frac{k_F^3}{3\pi^2}$ and t=|∇n|2φksn is a dimensionless density

gradient.

The function H was constructed to satisfy three conditions: H is given by its second-order gradient expansion in the slowly varying limit, H must approach $-\varepsilon_C^{unif}$ in the rapidly varying limit, the correlation energy must be a constant under uniform scaling to the high-density limit. Hence, the formula for H function can be written as

$$H = \left(e^2/a_0\right)\gamma\varphi^3 \ln\left[1 + \frac{\beta}{\gamma}t^2\left(\frac{1+At^2}{1+At^2+A^2t^4}\right)\right], \quad (19)$$

where A= $\frac{\beta}{\gamma}\left\{exp\left[\frac{-\varepsilon_C^{unif}}{\frac{\gamma\varphi^3e^2}{a_0}}\right] - 1\right\}^{-1}$.

The GGA for the exchange energy can be written as

$$E_X^{GGA} = \int \rho\varepsilon_X^{LDA}(\rho)F_X(s)d\boldsymbol{r}. \quad (20)$$

The formula of the function $F_X(s)$ that satisfies all requirements is

$$F_X(s) = 1 + k - \frac{k}{1+\frac{\mu s^2}{k}}, \quad (21)$$ where k=0.804.

2.2.3 LDA+U

Because LDA and GGA methods are built from the orbital-independent potentials, they fail to describe strongly correlated systems containing the transition metal or rare-earth metal ions with partially filled *d* or *f* shells. To overcome this, several methods such as the Hatree-Fock method [34], GW approximation [35], the self-interaction correction (SIC) method [36], and LDA+U

method [37] were proposed to incorporate the strong electron-electron correlations between *d* and *f* electrons. The total energy in the LDA+U method is given as:

$$E_{DFT+U} = E_{DFT} + E_U = E_{DFT} + E_{Hub} - E_{dc}, \quad (22)$$

where E_{Hub} is the corrective Hubbard functional and E_{dc} is the double-counting energy of the same electronic interactions. The simplified form for the total corrective energy is written as

$$E_U = E_{Hub} - E_{dc} = \sum_{I,\sigma} \frac{U^I}{2} Tr[n^{I\sigma}(1 - n^{I\sigma})], \quad (23)$$

where $n^{I\sigma}$ is the occupation matrix and U is determined by the effective on-site electronic interaction. U can be calculated from the linear-response theory [38]. At a higher level, the corrective energy is constructed from the extended Hubbard model with the on-site and inter-site electron interactions [39]. The total energy in this model is given as

$$E_{DFT+U+V} = E_{DFT} + \sum_I \frac{U^I}{2} Tr[n^I(1 - n^I)] - \sum_{IJ} \frac{V^{IJ}}{2} Tr(n^{IJ} n^{JI}), \quad (24)$$

where $n^{IJ\sigma}_{m,m'} = \sum_{k,v} f_{k,v} \langle \phi^I_m | \Psi^\sigma_{kv} \rangle \langle \Psi^\sigma_{kv} | \phi^J_{m'} \rangle$ and I, J are distinct atomic sites.

2.3 Beyond DFT -Hybrid Functional Methods

This group of methods is called "hybrid functionals" because they are the combinations of the orbital-dependent Hartree-Fock (HF) and an explicit density functional with different ratios. Up to now, these functionals are the most accurate methods for the calculation of exchange-correlation energy. These methods are successful partially thanks to the use of the HF exchange energy [40]. The hybrid functionals provide better formation energies of small molecules, accurate results of band gaps, and band structures. Several hybrid schemes origin from the adiabatic connection formula for the exchange-correlation energy [41]:

$$E_{XC} = \int_0^1 U_{XC}^{\lambda}\, d\lambda, \quad (25)$$

where $U_{XC}^{\lambda} = \langle \Psi_\lambda | V_{ee} | \Psi_\lambda \rangle - \frac{1}{2}\int\int \frac{\rho(\boldsymbol{r_1})\rho(\boldsymbol{r_2})}{|\boldsymbol{r_1}-\boldsymbol{r_2}|} d\boldsymbol{r_1} d\boldsymbol{r_2}$ and λ is an interelectronic coupling-strength parameter. This formula connects the non-interacting Kohn Sham reference system (λ=0) to the fully-interacting real system (λ=1) [42]. There are a lot of hybrid functionals that have been built to solve some specific problems. However, in the limit of this thesis, three functionals are presented: PBE0 -the basic functional, B3LYP -the most commonly used functional, and HSE06 -the functional that was used in our calculation.

2.3.1 PBE0 functional

The PBE functional is the combination of the ACM0 model and the PBE GGA and does not contain any adjustable parameter [43]. The exchange-correlation energy in PBE0 scheme is computed by the following formula

$$E_{XC}^{PBE0} = aE_X^{HF} + (1-a)E_X^{PBE} + E_C^{PBE}, \quad (26)$$

where E_X^{HF} is the exchange energy in the Hartree-Fock model, E_X^{PBE} and E_C^{PBE} are the exchange and correlation energies in PBE GGA method, respectively, and $a = \frac{1}{4}$ is determined by the perturbation theory. The nonlocal Fock exchange energy is given as,

$$E_x = -\frac{e^2}{2}\sum_{kn,qm} 2w_k f_{qm} \times \int\int d^3\boldsymbol{r} d^3\boldsymbol{r'} \frac{\boldsymbol{\phi}^*_{\boldsymbol{kn}(r)}\boldsymbol{\phi}^*_{\boldsymbol{qm}}(\boldsymbol{r'})\boldsymbol{\phi}_{\boldsymbol{kn}}(\boldsymbol{r'})}{|\boldsymbol{r}-\boldsymbol{r'}|}, \quad (27)$$

where $\boldsymbol{\phi}_{\mathbf{kn}}(\boldsymbol{r})$ is a set of one-electron Bloch states of the system and $f_{\mathbf{kn}}$ is the corresponding set of occupation numbers. The sums over **k** and **q** run overall k-points and the sums over *m* and *n* run overall occupied bands. The PBE0 functional shows its strength in calculations of molecular structures and properties along with the whole periodic table. Furthermore, this model can be

applied to very large systems due to the linear scaling implementations.

2.3.2 B3LYP functional

The B3LYP model was proposed by Axel D. Becke in 1993 [44,45]. It is the combination of the Becke88 exchange part and the Lee-Yang-Parr correlation part. The explicit formula is written as:

$$E_{XC}^{B3LYP} = E_{XC}^{LDA} + a_0(E_X^{HF} - E_X^{LDA}) + a_x(E_X^{GGA} - E_X^{LDA}) + a_c(E_C^{GGA} - E_C^{LDA}),$$

(28) where $a_0 = 0.20, a_x = 0.72, and\ a_c = 0.81$.

Several tests of B3LYP on geometrical parameters, bond length, barrier heights, thermochemistry, and ionization potential have been made. Recently Riley *et al.* [46] compared the determination of bond lengths of six functionals (Slater, SVWNV, BLYP, B3LYP, and c-SVWNV); the results gave the remarkable plus of B3LYP that it provides the best outputs. Similarly, the efficiency of barrier-height calculations for 23 reactions was checked using 37 density functionals by Riley *et al.* [47], B3LYP was the second-best method for this computation. However, for the thermochemistry performance, a comparison done by Schultz *et al.* [48] shows that B3LYP of which result accuracy was ranked 27th out of the 42 functionals cannot perform the calculations of atomization energies well. Another drawback of B3LYP model is its ability to simulate the ionization potentials. The work done by Zhao *et al.* [49] obtained the second-worst results from B3LYP for the ionization potentials of a dataset comprising six atoms and seven molecules. Although B3LYP demonstrates some disadvantages, due to its availability to various chemical systems, this method is the most used of all functionals [50].

2.3.3 HSE functional

HSE functional was proposed by J. Heyd, G. E. Scuseria, and M. Ernzerhof (HSE) in 2003 [51]. This hybrid functional is based on a screened Coulomb operator for the exchange interaction. It makes the exchange hole localized among the near neighbors of a reference point, but not beyond. The idea of this model originates from the separation of electron-electron interaction into two parts, short-range and long-range interactions [52-55].

$$\frac{1}{r_{ij}} \equiv \frac{erf(\mu r_{ij})}{r_{ij}} + \frac{erfc(r_{ij})}{r_{ij}}, \tag{29}$$

where $\frac{erf(\mu r_{ij})}{r_{ij}}$ is the long-range and $\frac{erfc(r_{ij})}{r_{ij}}$ is the short-range?

The exchange term in the PBE0 model is split into short-and long-range components:

$$E_X^{PBE0} = aE_X^{HF,SR}(\omega) + aE_X^{HF,LR}(\omega) + (1-a)E_X^{PBE,SR}(\omega) + E_X^{PBE,LR}(\omega) - aE_X^{PBE,LR}(\omega) \tag{30}$$

Because numerical test indicates that the HF and PBE long-range exchange parts cancel each other and have a very small contribution they are neglected in the energy calculation. Thus, the HSE functional has the form of:

$$E_{XC}^{\omega PBEh} = aE_X^{HF,SR}(\omega) + (1-a)E_X^{PBE,SR}(\omega) + E_X^{PBE,LR}(\omega) + E_C^{PBE}, \tag{31}$$

where ω is an adjustable parameter governing the extent of short-range interactions. When ω=0, the HSE functional becomes the PBE0, and when ω→∞, the HSE tends to reach the PBE form. From the HSE form in Eq. 2.29, two functionals HSE03 and HSE06 were derived. The only difference between the two forms is the ω value. In HSE03, ω=0.15$a0-$, while in HSE06, ω has

two values, ω=0.15/√2 for Hartree-Fock and ω=0.15×2 /3 for the PBE part [56]. The HSE functional shows the accuracy, performance comparable to the best hybrid methods, such as B3LYP and PBE0. Especially, in the computational point of view, this model shows better efficiency. It can provide significant reductions in computational effort. Furthermore, it can be applied to a variety of chemical systems.

2.4. Nudged Elastic Band Method

Nudged elastic band (NEB) is a method to find a minimum energy pathway (MEP) between a pair of stable states [57]. In this method, a string of images is used to describe a reaction pathway. To keep spaces between images equal along the reaction path, those images are connected by spring forces. To start the NEB calculation, an initial pathway between initial and final states must be chosen; typically, a linear pathway is sufficient. Two forces that exert on the images to pull them into relaxation points are potential force acting perpendicular to the band and spring force acting along the band. The NEB force exerting on the *i*-th image is

$$\boldsymbol{F}_i^{NEB} = \boldsymbol{F}_i^{\perp} + \boldsymbol{F}_i^{S\parallel}, \quad (32)$$

where $F_i^{\perp}$ is the perpendicular force due to the potential

$$\boldsymbol{F}_i^{\perp} = -\nabla(\boldsymbol{R}_i) + \nabla(\boldsymbol{R}_i).\hat{\boldsymbol{\tau}}_l\hat{\boldsymbol{\tau}}_l$$

and $\boldsymbol{F}_i^{S\parallel}$ is the spring force,

$$\boldsymbol{F}_i^{S\parallel} = k(|\boldsymbol{R}_{i+1} - \boldsymbol{R}_i| - |\boldsymbol{R}_i - \boldsymbol{R}_{i-1}|)\hat{\boldsymbol{\tau}}_l$$

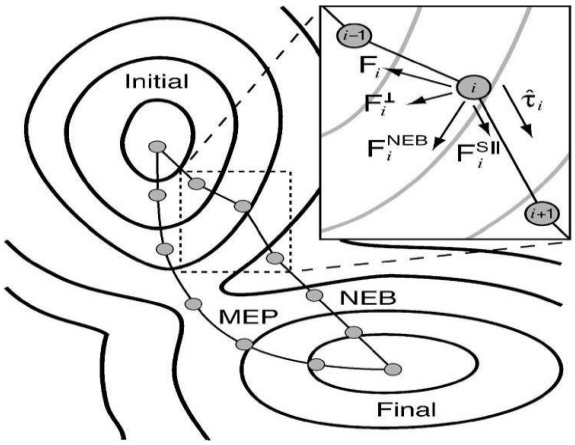

Fig 2. 1 Forces acting on the i-th image are described in detail. The nudged elastic band force $\boldsymbol{F_i^{NEB}}$ *is made up of two forces: the spring force* $\boldsymbol{F_i^{S\parallel}}$ *lying along the tangent* $\hat{\boldsymbol{\tau}}_l$ *and the potential force* $\boldsymbol{F_i^{\perp}}$ *acting perpendicular to the band. (D. Sheppard, R. Terrell, and G. Henkelman J. Chem. Phys. 128 (2008) 134106)*

It is important to find the saddle point because the difference between the saddle-point energy and initial-state energy is the reaction barrier and by minimizing the saddle point, the MEP can be obtained. The saddle point can be found efficiently by two steps: the first step is to optimize an NEB calculation and the second step is to do a min-mode following saddle point search. Another method to find the saddle point is the climbing-image (CI-NEB). By a reflection in the force along the tangent, the highest energy image *l* with zero total spring force climbs to the saddle point.

$$F_l^{Cl} = F_l - 2F_l\hat{\boldsymbol{\tau}}_l\hat{\boldsymbol{\tau}}_l. \quad (33)$$

2.5. Plane Wave Basis Set

A PW basis set for states of wave vector k is defined as

$$\langle r|\boldsymbol{k}+\boldsymbol{G}\rangle = \frac{1}{\sqrt{\mathrm{N}\Omega}} e^{i(\boldsymbol{k}+\boldsymbol{G}).\boldsymbol{r}}, \frac{\hbar^2}{2m}|\boldsymbol{k}+\boldsymbol{G}|^2 \leq E_{cut} \quad (34)$$

Ω = unit cell volume, NΩ = crystal volume, Ecut = cutoff on the kinetic energy of PWs (to have a

finite number of PWs!). The PW basis set is complete for $E_{cut} \rightarrow \infty$ and orthonormal: $\langle k+G|k+G'\rangle = \delta_{GG'}$

The components on a PW basis set are the Fourier transform:

$$|\psi_i\rangle = \sum_G c_{i,k+G}\,|k+G\rangle \quad (35a)$$

$$c_{i,k+G} = \langle k+G|\psi_i\rangle = \frac{1}{\sqrt{N\Omega}}\int \psi_i(\boldsymbol{r})e^{-i(k+G).\boldsymbol{r}}d\boldsymbol{r} = \widetilde{\psi_i}(k+G).| \quad (35b)$$

Since PWs are not practical basis set for electronic structure calculations for instead from simple Fourier analysis: length scale δ → Fourier components up to q ~ 2π/δ. In a solid, this means ~ $4\pi\frac{\left(2\pi/\delta\right)^3}{3\Omega_{BZ}}$PWs (volume of the sphere of radius q divided by $\Omega_{BZ} = \frac{8\pi^3}{\Omega}$, volume of the Brillouin Zone). Estimate for diamond: 1s wavefunction has $\delta \simeq 0.1\ a.u., \Omega = \frac{(2\pi)^3}{\left(a_0^3/4\right)}$ with lattice parameter a_0 = 6.74 a.u. → 250, 000 PWs! Hence not practical therefore We need to:

• get rid of core states

• get rid of orthogonality wiggles close to the nucleus

To achieve the above, we need a pseudopotential (PP)

2.6. Pseudopotential

It is a smooth effective potential that reproduces the effect of the nucleus plus core electrons on valence electrons. Smoothness and transferability are the relevant keywords:

• We want our pseudopotential and pseudo-orbitals to be as smooth as possible so that expansion into plane waves is convenient (i.e. the required kinetic energy cutoff is small)

• We want our pseudopotential to produce pseudo-orbitals that are as close as possible to true ("all-

electron") orbitals outside the core region, for all systems containing a given atom (in the fig 2.2: all-electron and pseudo-orbitals for Si). Of course, the two goals are usually conflicting! Pseudopotentials have a long story: let's start from the end.

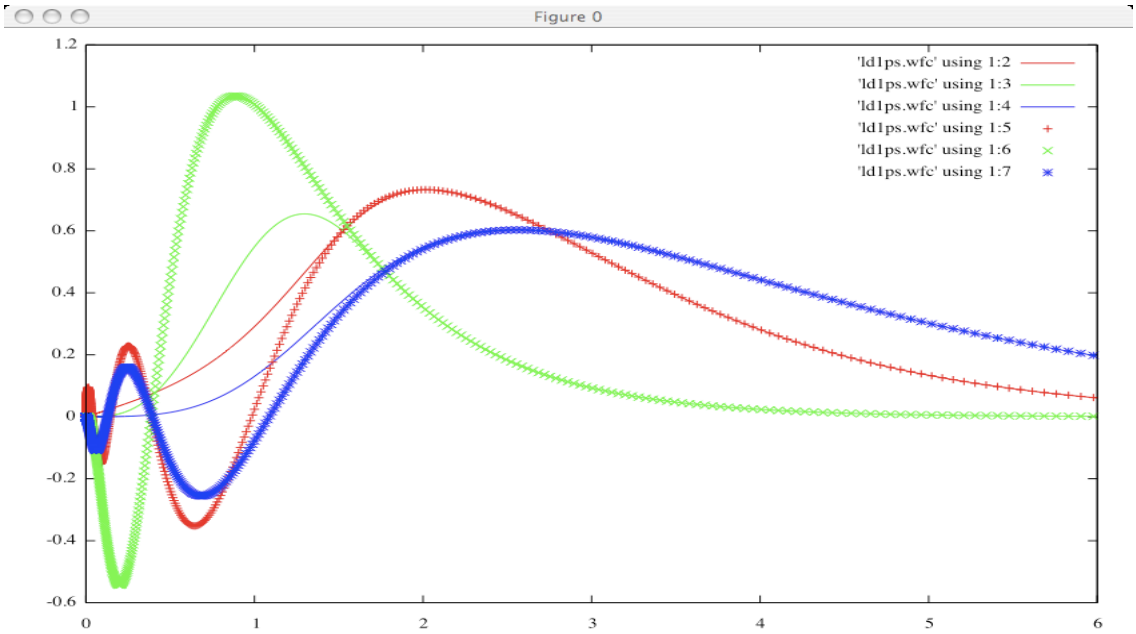

Fig 2. 2 Pseudopotential showing all electrons in star (*) and pseudo-electrons in line [40].

2.6.1 Projector-Augmented Wave (PAW)

Let us look for a linear operator $\hat{T}$ connecting all-electron orbitals $|\psi_i\rangle$ to pseudo-orbitals $|\tilde{\psi}_i\rangle$ as in: $|\psi_i\rangle = \hat{T}|\tilde{\psi}_i\rangle$. Pseudo-orbitals will be our variational parameters. We write the charge density, energy, etc. using pseudo-orbitals and $\hat{T}$ instead of all-electron orbitals. The operator $\hat{T}$can be defined in terms of its action on atomic waves (i.e. orbitals at a given energy, not necessarily bound states):

• $|\phi_l\rangle$: set of atomic all-electron waves (bound or unbound states)

• $|\tilde{\phi}_l\rangle$: a corresponding set of atomic pseudo-waves. Beyond some suitable "core radius" $R_l, \tilde{\phi}_l(r) = \phi_l(r)$; for $r < R_l, \tilde{\phi}_l(r)$ are smooth functions.

If the above sets are complete in the core region, the operator $\hat{T}$ can be written as

$$|\psi_i\rangle = \hat{T}|\tilde{\psi}_i\rangle = |\tilde{\psi}_i\rangle + \sum_l \left(|\phi_l\rangle - |\tilde{\phi}_l\rangle\right) \langle\beta_l|\tilde{\psi}_i\rangle \quad (36)$$

where the β_l "projectors" are atomic functions, having the properties $\langle\beta_l|\tilde{\phi}_m\rangle = \delta_{lm}$ and $\beta_l(r) = 0$ for $r > R_l$

The pseudopotential itself is written as a nonlocal operator $\hat{V}$, in terms of the β_l projectors:

$$\hat{V} = V_{loc}(r) + \sum_{lm} |\beta_l\rangle D_{lm} \langle\beta_m| \quad (37)$$

(V_{loc} contains the long-range Coulomb part $-Z\frac{e^2}{r}$).

2.6.2 Type of pseudopotential

2.6.2.1 Norm-conserving:

+ are simple to generate and to use. Theory and methodological improvements are invariably implemented first (and often only) for norm-conserving PPs.

– are relatively hard: core radii R_l cannot exceed by much the outermost maximum of the valence atomic orbitals, or else the loss of transferability is large. For some atoms: 2p elements C, N, O, F, 3d transition metals, 4f rare earth, this restriction may lead to very high plane-wave cutoffs (70 Ry and up).

– do not give any sensitive information about the orbitals close to the nucleus (all-electron orbitals can be "reconstructed" using the PAW transformation). This is usually your first choice and starting point.

2.6.2.2 Ultra-soft:

+ can be made smooth with little loss of transferability: core radii Rl can be pushed to larger values, even for "difficult cases". Cutoffs of 25 to 35 Ry are usually good for most cases. Note that you may need a second FFT grid for augmentation charges, with typical cutoff 8÷12× orbital cutoff (instead of 4)

- are not simple to generate: the pseudization of augmentation charges is often a source of trouble (e.g. negative charge)

- introduce additional terms in the formalism: some property calculations may not implement

– give even less information about the orbitals close to the nucleus (all-electron orbitals can be "reconstructed")

Ultra-soft PPs are typically used in all cases where norm-conserving PPs are too hard: C, N, O, F, 3d elements, "semi core" states

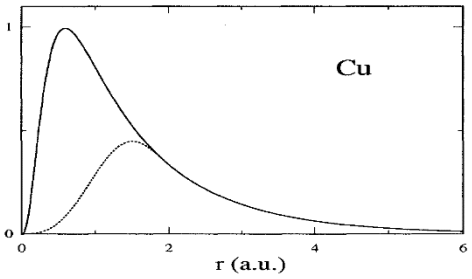

Fig 2. 3 Norm-conserving and semi core states pseudopotential

2.6.2.3 Projector- Augmented Wave (PAW)

It's most transferrable, even for atoms that are "difficult" for Ultrasoft PPs (e.g.magnetic materials): accuracy is comparable to all-electron techniques (e.g. FLAPW). It gives information about the orbital close to the nucleus, as complex to generate as Ultrasoft PPs, introduces even more additional terms in the formalism: some property calculations may not implement. There is a few more aspect to be considered in the choice of a pseudopotential:

• PPs are bound to a specific XC functional, at least in principle. Exception: Hybrid, nonlocal (vdW-DF), meta-GGA functionals, for which very few (or no) PPs are available. Typically, PPs computed from the most similar GGA are used instead.

• The distinction between "core" and "valence" electrons is not always clear-cut. In some cases, you may need to extend "valence" to include the so-called semi core states to achieve better (or less lousy) transferability. E.g.: 3d states in Zn and Ga; 3s and 3p states in 3d transition metals Fe, Co, Ni.

The inclusion of semi core states adds considerable complexity to both the generation and the practical usage of a PP: to be done only if need be. There are many ready-to-use PPs tables around, but there is not a single standard PP file format: each code has its format.

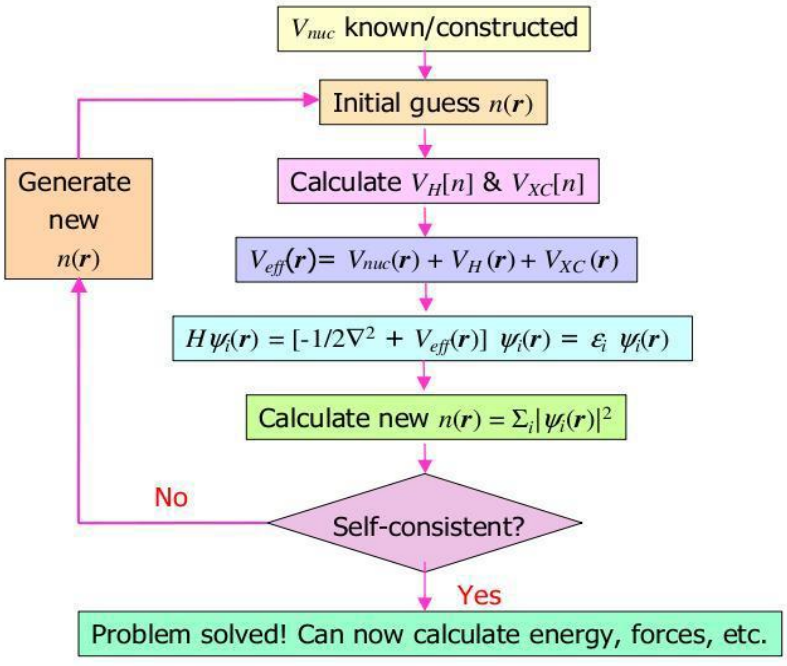

Fig 2. 4 schematic for self-consistency calculation on Density Functional Theory (DFT)

CHAPTER THREE

3.0 METHODOLOGY

3.1 COMPUTATIONAL METHODS

We used Quantum Espresso *ab initio* simulation package with the projected-augmented-wave (PAW) method and the GGA/PBE functional [40-42] of the exchange-correlation energy of electron for first-principles calculations presented here to get insights into superior sodium-ion storage performance of the porous carbon. The energy cutoff on PW bases was set at 400 eV, and the threshold of self-consistency convergence was set to $1x10^{-8}$ eV and that enforce at 0.01 eV $Å^{-1}$ in structured relaxation. In the computations, integrating into the unit cell of reciprocal space was sampled at gramma point for supercell electronic smearing of occupation numbers of electronic states ($\sigma = 0.2$eV) was used.; cell shape and volume were kept fixed. Projected electronic densities of states were obtained from the Kohn-Sham wavefunctions by projection onto local orbitals of valence s and p states. In this study, DFT was employed to calculate the adsorption energy or binding energy of an atom in the host material. However, the adsorption energy informed us of how many numbers of the atoms will be stored in the structure. Therefore, sodiation and lithiation $E_{M(x)}$ energies were defined to evaluate how many metals (Na, Li, and Mg) Na atoms can be stored within the porous carbon structure at low without considering the effects of the temperature and entropy. The energetics of Na, Li, and Mg insertion in the porous carbon structure were computed based on the binding energies per Na, Li, and Mg atoms E_b

$$E_b = \frac{E_{S-M} - E_S - XE_M}{X}, \qquad (38)$$

Where $E_{(S-M)}$ is the energy of the porous carbon intercalating x M (M= Na, Li, Mg) atoms within it, E_S is the energy of porous structure, and E_M is the cohesive energy of bulk metal per atom (Na,

Li, Mg). An average adatom intercalation potential can be obtained directly from the differential of the adsorption energy and the cohesive energy of the metal (Na, Li, Mg) from

$$V_{ave} = -\frac{E(b)-E(M_{cohesive})}{x.e}, \quad (39)$$

Where E(b) is the binding/adsorption energy per atom inserted, $E(M_{coshesive})$ is the cohesive energy of M (M = Na, Li, Mg), x is the number of adatom and e is the electron charge.

Ideally, Gibbs's free energy ($G_x = \Delta E + P\Delta V - T\Delta S$) should be used in the calculation of average voltage. However, since PΔV and TΔS are typically negligible compared to the energy term ΔE, we only consider the energy in our analysis.

Anode capacity is a measure of charge that can be stored in a material and it is an important parameter to evaluate the performance of storage devices. Here, we focus on the specific capacity which is more useful in studies of materials. The theoretical specific capacity C of an electrode is estimated using:

$$C = \frac{n_i N_A n_e e}{M}, \quad (40)$$

Where n_i is the number of intercalated ions, N_A is the Avogadro constant, n_e is the valence of an ion, e is the electric charge of an electron, and M is the molar mass of the structural model.

3.2 STRUCTURAL MODEL OF POROUS CARBON

We use a method of expanded lattice constant approach. Motivated by its extensive use in studies of amorphous materials [1]. In our initial application, we noticed that yields porous structures when used at low densities. Hence, we decided to systematize our procedure by expanding the diamond lattice in three directions to match the density of porous carbon. This was done by considering a

cubic unit cell of edge length a; all the sides were expanding by a factor $n^{1/3}$ which will correspondingly increase the inter-atomic distances and the volume will become a 3n. If n is larger than 1 the final density will be smaller than the initial.

In dealing with the ab initio simulation of porous carbon the following procedure was carried out. We first considered the conventional cubic unit cell of diamond structure with periodic boundary conditions containing 8 atoms, a = 4.543 Å Then the volume of the unit cell was doubled by increasing the cell edge a to $2^{1/3}$a and the interatomic distances increased accordingly. Since the structure obtained in this manner is unstable, we performed optimization calculation after distorting the structure internally using the eigenvector of the unstable modes in a 2x2x2 supercell (Fig 3.1a) containing 64 atoms optimized lattice constant are a = 9.086 Å, 8.835 Å, 8.6095 Å with densities of 1.702 g/cm^3, 1.85 g/cm^3 and 2.0 g/cm^3 respectively.

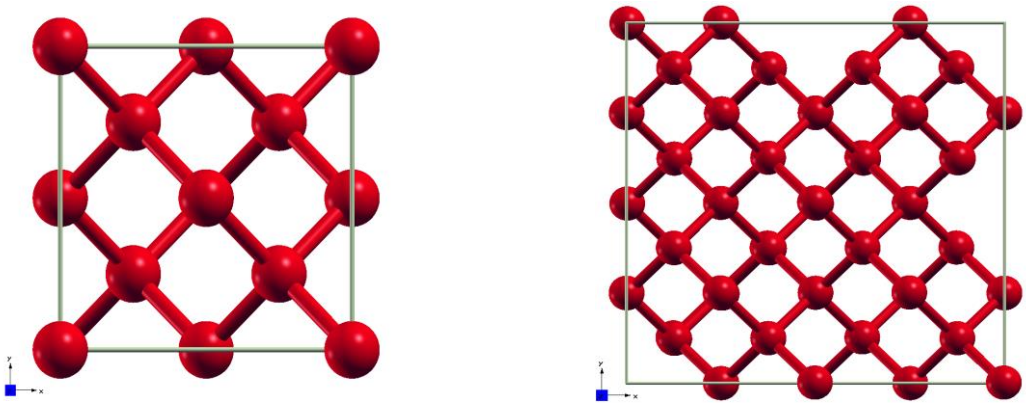

Fig 3. 1(a) unit cell of a diamond structure (b) 2x2x2 supercell of internally distorted diamond structure

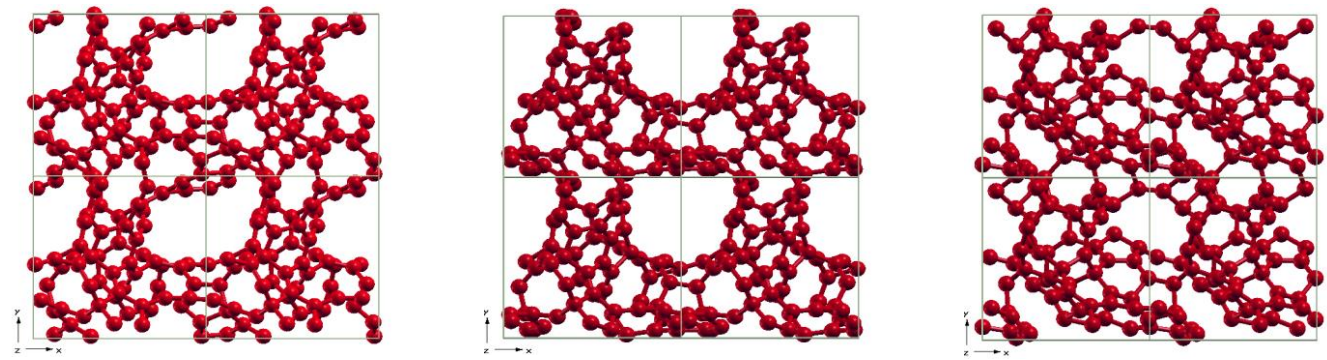

(a) (b) (c)

Fig 3. 2model structure of Porous carbon of densities (a) 1.70 g/cm^3, (b) 1.85 g/cm^3 and (c) 2.0 g/cm^3 after DFT calculations

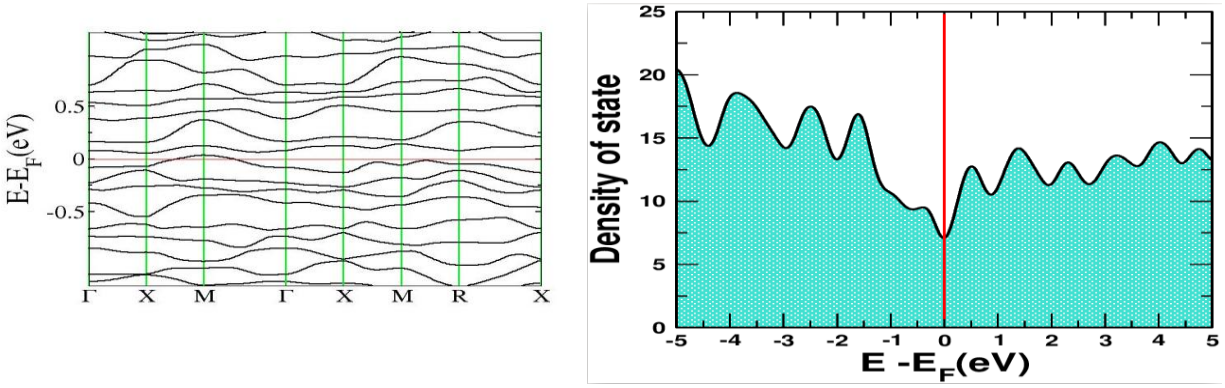

Fig 3. 2a Electronic structure of the modeled porous carbon showing that the porous carbon is a P-type semiconductor where holes are contributing to the conductivity of the modeled structure

Fig 3. 2b3 The density of state for the modeled porous structures is localized near EF indicate that electron hopping between localized state is required.

CHAPTER FOUR

4.0 RESULTS AND DISCUSSION

4.1 Porous carbon structure

Three model periodic structures of porous carbon structures we generated in this work at the densities of 1.70, 1.85 and 2.0 g/cm^3 are shown in Fig.3.2 b-c. We considered these different structures to ensure that our results are not sensitive to a choice of particular structure generated using our method. The bond length distribution shown in Fig.4.2 is in good agreement with that obtained from the neutron diffraction experiments reported [53]. All the three-model structure of porous carbons have sp^3 carbon fraction of approximately 50% in agreement with amorphous structure generated by melting and quenching MD [53]. Their fractional sp^3 character is related to a coordination number of approximately 3.5. Our model covers a wide parameter space of structure and densities as seen in fig.3.2a-c, we have 3, 4, 5, 6, 7 rings which is a measure for structural order [54]. The 50% fraction of sp^2 hybridized bonding in our structures makes it easy for a metal atom to intercalate into the porous material. Using POREBLAZER 3.0.2 software we obtained insight into the nature of the pores in the three structural model shows that our structure contains a channel with disorder edges into which metal atoms (Na, Li, Mg) can easily intercalate.

The bond distribution analysis (BDA) of nano porous carbon obtained by the expanding lattice method was done using Avogadro's software from the analysis we found that our model structures has three prominent peaks and a well-defined minimum between the first and the second peak; the distance at the minimum is the value used to define a bond between nearest neighbors. When one looks at the first peak of the carbon BDA in more detail (Fig.4.2) the following features appear.

There are three peaks that may be associated to three different bonding states: single bonds (1.45 Å), with respect to the crystalline diamond-like value of 1.54 Å, but close to the interatomic distance in graphite,1.41 Å; double bonds at 1.35 Å, to be compared with 1.34 Å for C=C; triple bonds at 1.15 Å, to be compared with 1.20 Å for C≡C [6]. The number of nearest neighbors with no multiple bonds, is determined by the corresponding height at r = 1.45 Å, is larger than the rest, which indicates that they may be located mainly within the bulk forming graphitic rings, whereas the atoms with double bonds and triple bonds are mainly located on the surfaces of the pores since the pores are small compared to the backbone.

(a) *(b)* *(c)*

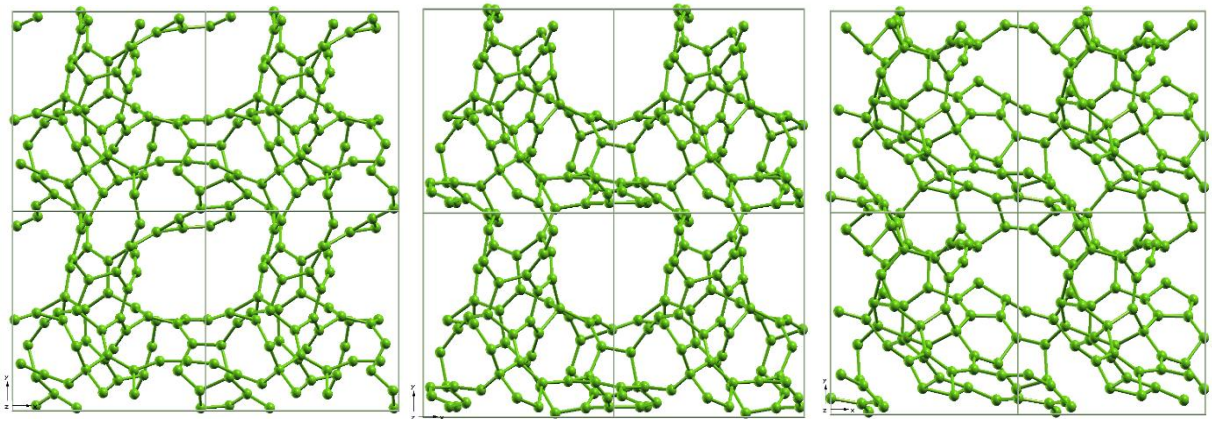

Fig 4. 1 model structure porous carbon of densities of 1.7 g/cm^3 (a), 1.85 g/cm^3 (b) and 2.0 g/cm^3 (c) derived from first-principles DFT simulations. These structures contain both odd and even membered rings up to 7-member ring

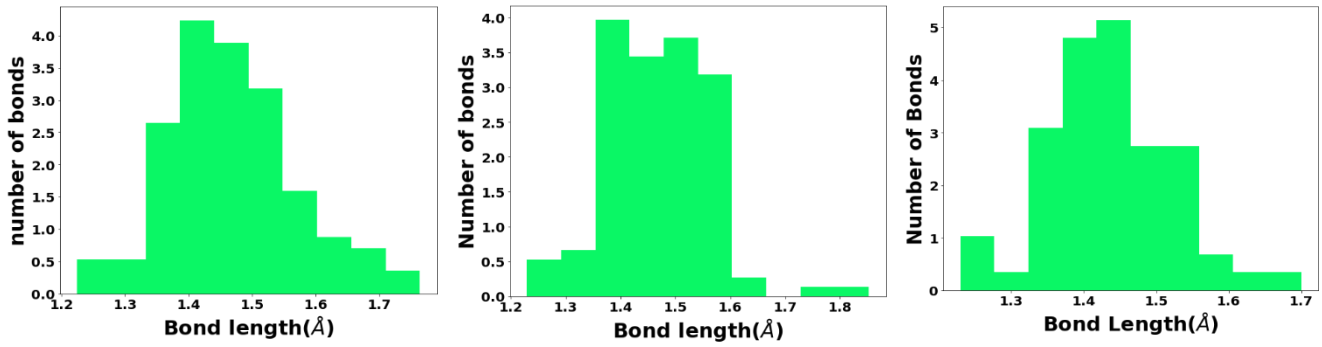

Fig 4. 2 Distribution of bond length in the model structures of porous carbon having densities 1.7 g/cm^3(a), 1.85 g/cm^3(b) and 2.0 g/cm^3(c).

4.2 Intercalation energetics of Na, Li and Mg in porous carbon

Using the optimized porous carbon structures in (Fig.4.1), we determined energetics of insertion of metals atoms (Na, Li, Mg) with DFT simulation adding of atoms into the porous structures. Due to porous nature of our models and availability of a channel sub structure, we sample several configurations generated randomly by adding metal atoms one after another optimizing the structure to get the binding energy of the adatoms. Our structural model contains a range of structural motifs such as odd-membered rings and open porous which are expected to facilitate adsorptions and affect clustering of metals (Na, Li, Mg) atoms. Binding energies of Na, Li and Mg in these structures are listed in (Fig. 4.4). It is reported in Ref 53 that the binding energies of Na insertion into graphite are +0.76 eV making it thermodynamically unstable hence Na does not intercalate into graphite. Amorphization of carbon makes Na insertion thermodynamically favorable with most sites in the three-models here showing binding energies stronger than the cohesive energy of Na. Thus, porous carbon of this kind can be useful as an anode in Na-ion batteries. In Fig. 4.4, we find out that the structural model with a lower density (1.7 g/cm^3) has

negative binding energy at most of the sites compared to higher densities of 1.85g/cm^3 and 2.0 g/cm^3. This is because the sp^2/sp^3 hybridized bonding reduces at higher densities, which implies low Na- intercalation. Hence, a porous carbon with low density is more favorable as an anode in Na-ion batteries. Insertion at higher concentration of Na, Li and Mg in the three structural models involve a positive binding energy giving a cap on capacity of storage.

We compare our voltage profiles with experimental observation of approximately 1.2 to 0.1 being a sloping region and a plateau region around 0.1 to 0.0 V vs Na resulting to a total capacity of 250 to 400 mAhg^{-1} depending on the nature of carbon [54]. Our theoretical estimate of voltages *A* associated with *B* insertion of a single atom of *C* Na are consistent with the sloping region and threat

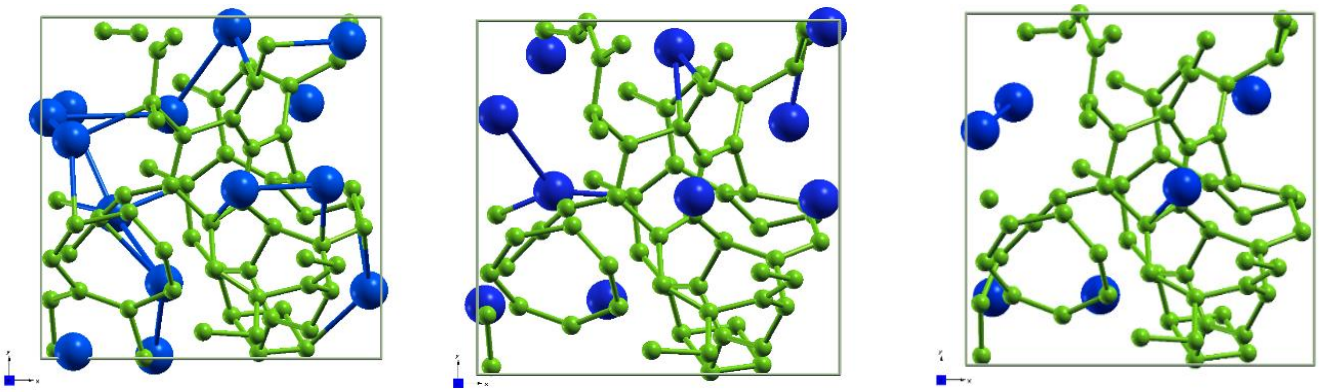

Fig 4. 3 Intercalation of Na atoms (blue) into the model structure of porous carbon of density the 1.70 g/cm^3 with increasing Na concentration from 15% weight in (A), 23% weight in (B) and 30% weight in (C). Further increase in Na intercalation is seen to result in clustering of Na atoms with no contribution of charge storage in the system.

Higher concentration of Na atom in the porous carbon are consistent with the plateau region (Fig. 4.5) and the observation of Na^+ is also consistent with diamagnetic ions seen by NMR [55].

The Na, Li and Mg adsorption on the models was a calculated. Similar to the Li and Mg atoms adsorption, Na adsorption is most stable with 1.7 g/cm^3 density model, when one or two Na atoms are adsorbed on the surfaces (Fig. 4.3). However, the Na adsorption is much weaker than that of the Li and Mg atom. This means that Na adsorption on the edge is not as stable as the Li adsorption in higher density porous carbon. When 6 Na atoms are adsorbed on the surfaces, the model with density of 1.7 g/cm^3 is more stable than Na in 1.85 and 2.0 g/cm^3, contrasting with the Li adsorption since the radius of the Na atom is larger. When more than 6 Na atoms are adsorbed on the possible sites, they get located near the surfaces through other Na atoms and on the hexatomic rings near the disorder surface, similar to the case of the Li atoms explain in [55]. The dependence of the sodiation energy (E_{Na}) on the number of the adsorbed Na atoms, very similar to that of the Li atom adsorption, is shown in Fig. 4.4 The minimum E_{Na} is reached when 10 Na atoms are adsorbed, again due to the larger radius of the Na atom.

In general, the sodiation energy is higher than the lithiation energy due to the weaker interaction between the carbon framework and the Na atom compared to Li and Mg atoms, this is seen from the positive absorption energy of Na shown in Fig. 4.4

Similarly, the voltage profile of the Li and Mg is higher than that of Na. The voltage decays sharply in all the three structural models from 3.35 V to 0.38 V when few atoms of Na, Li, and Mg are adsorbed, when more than 6 Na, Li and Mg atoms are adsorbed, the voltage curve become flat (i.e below 0.38 V). Its minimum is reached when 10 Na atoms are adsorbed. Finally, metallic sodium is formed and the voltage becomes very close to zero with 14 Na atoms clustering at the surface of the rings structure.

There are two opposite interpretations on the sloping and low potential plateau regions of a discharge profile of the porous hard carbons as the Li or Na ions can be intercalated in to the micro graphene layers and adsorbed on/in the pores, the so-called intercalation ↔ adsorption mechanisms. On studying the Li and Na storage performance of pyrolyzed glucose, Dahn et al. [55] attributed the high-potential sloping region to the intercalation of the Li or Na ions and the plateau region to the adsorption and adsorption/deposition within the micropores. Such recognition was later supported by Komaba et al. [44] and Tarascon et al. [45]. More authors, however, believed that the sloping region corresponds to the adsorption of the Li or Na ions while the plateau is for the ion intercalation and deposition of the metals [46-48]. It seems that each proposed mechanism was supported with solid experimental evidence. The above calculations show that, depending on the number of Li or Na atoms adsorbed on the surfaces, the discharge (lithiation or sodiation) voltage varies in a wide range, covering both the adsorption and intercalation types of the Li or Na storage in carbon. Therefore, we believe that it is difficult to judge which part of a discharge profile represents the adsorption or intercalation of the Li or Na atoms, simply by the shape of the discharge voltage profile alone, though we believe that the sloping region receives more contribution from the adsorbed ions [53].

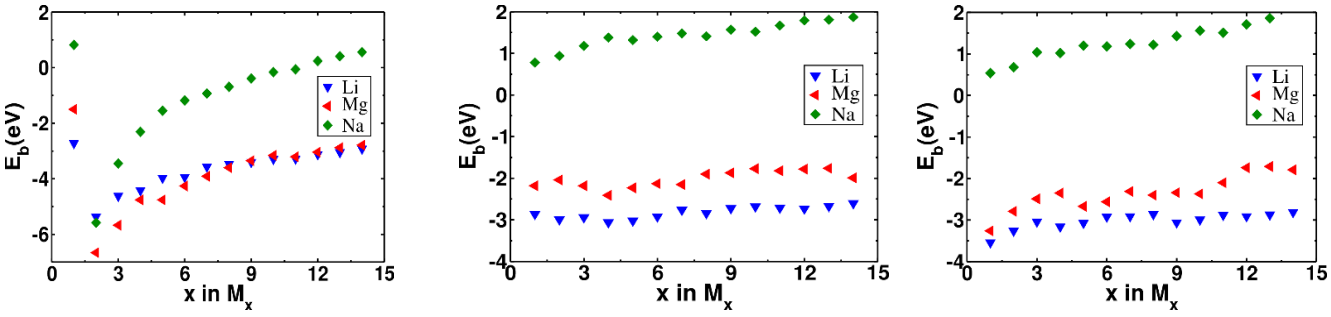

Fig 4. 4 Energy of binding of Li, Na, and Mg atoms intercalated into the three structural models of porous carbon of densities 1.7 (a), 1.85 (b), 2.0 (c) g/cm3 as a function of concentration Na(green), Li(blue), Mg(red).

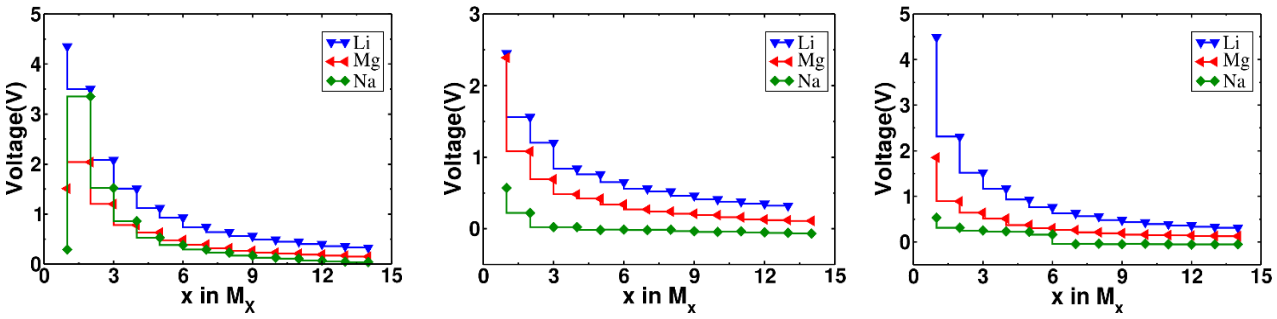

Fig 4. 5 Voltage profile of the three structural models of density 1.7 (a), 1.85 (b), and 2.0 (c) g/cm^3 respectively in which Na, Li, Mg atoms have been inserted with their voltages shown as we increase the number of atoms Na(green), Li(blue) and Mg(red).

4.3 Electronic structure

Electronic structure was analyzed to understand the insertion of Na, Li, Mg into our structural models (Fig. 4.6). Show atomically resolved electronic densities of states (DOS) of Na, Li Mg atoms showing data from low to high filling with the present of defect and disorder, carbon systems from such simulations exhibits a finite DOS contribution by the metal atoms are all above the fermi level. This correspond to an unfilled s valence orbital and therefore to an ionic state in all three cases (Na^+, Li^+, Mg^{2+}). With increasing filling, larger contributions below the Fermi level are seen in the projected DOS for the metal atoms. Such mechanism has been previously discussed for Li on graphene [54] and Na in a porous carbon model system [54]. Our work based on the same porous carbon framework for intercalation of Na, Li and Mg suggests the cross-over from ionic to metallic nature to be a universal feature of all three metal species being intercalated into porous carbon materials.

We probed different fillings in the same host structure and computed the partial electronic density of states (PDOS) at each stage. Initially, a single inserted Na, Li, and Mg transfers its valence charge to carbon framework completely, forming Na^+, Li^+ and Mg^{2+} and the 3s orbital of the metal atoms remains unoccupied above the Fermi level. With increasing filling, occupied Na, Li and Mg levels occur first with a zero, then with a finite partial DOS directly at Fermi level. A closer look at the case with largest filling reveals distinct differences between individual Na, Li, Mg sites. Indeed, lower Na, Li, Mg charges are observed with increasing occurrence of Na-Na, Li-Li and Mg-Mg contacts in the nearest-neighbor shell.

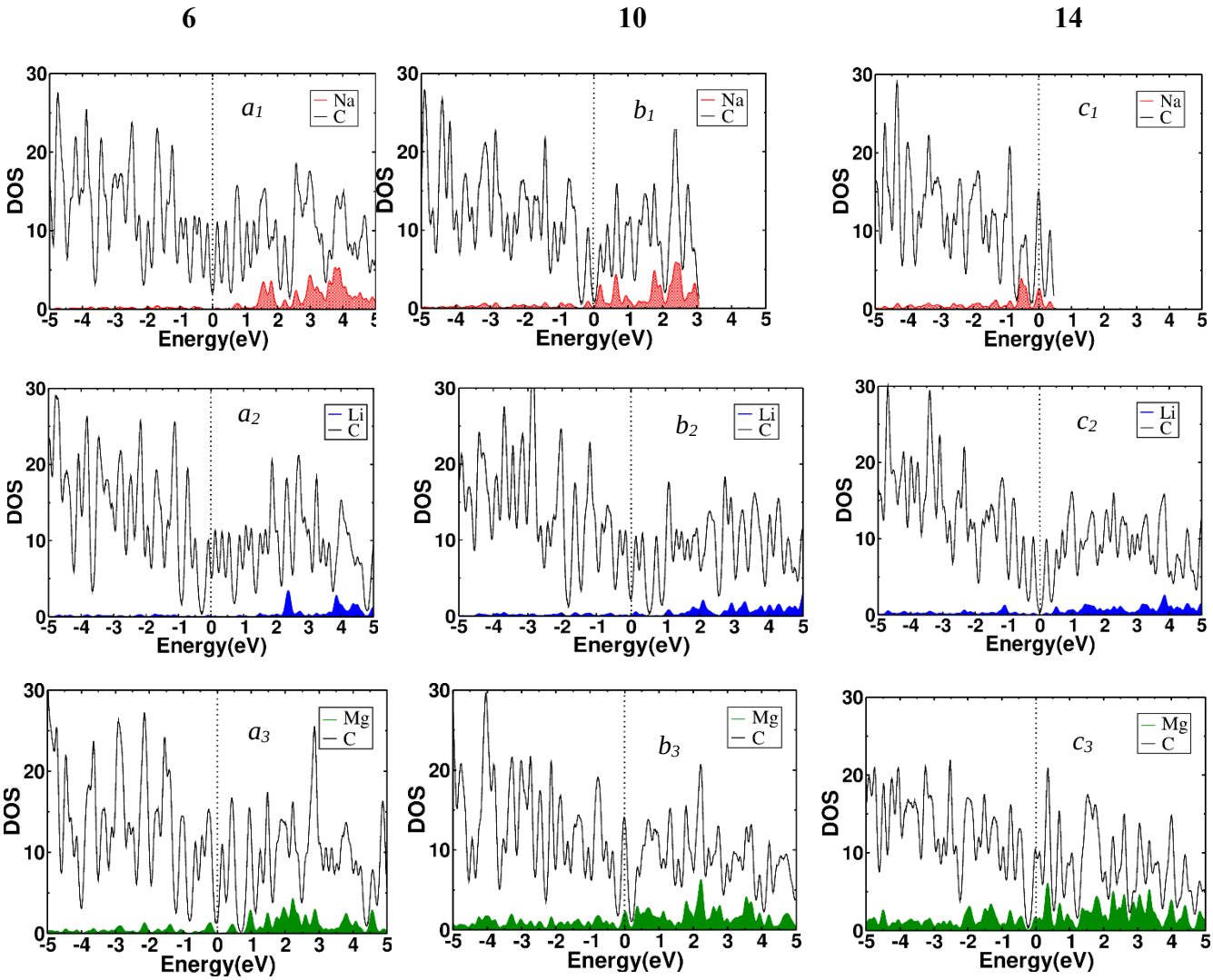

Fig 4. 6 Electronic densities of states (DOS), computed within DFT and atomically resolved by projection onto atomic orbital basis providing electronic picture of ion-C intercalation at various degrees of interaction. Projection onto the C atoms (grey) and metal atoms are shown for Na(red), Li(blue) and Mg(green) respectively. The fermi level is set E = 0, and indicated by a vertical dashed line. (a) is 6 adatoms into our structural model of porous carbon showing that metal atoms transfer electronic charge to the porous carbon and become Na^{+} (top), Li^{+} (middle) and Mg^{2+}(bottom) with no Na, Li and Mg orbital occupancy below the Fermi level. In (b), there is weak occupancy of ionic orbital below the Fermi level. As we increase the number of metal atoms to 10 (c), there is clustering of the metal atoms and hence no reduction in the state of occupancy above the Fermi level except Na (c1) as the number of adatoms increased to 14.

CHAPTER FIVE

5.0 CONCLUSIONS

Three densities structural models of hard carbon were constructed to understand the Na, Li and Mg atom intercalation on the porous carbon. We find that the energies of Na atoms binding at most sites are negative for lower density model and positive in all the absorption sites for higher densities structural model of 1.85 g/cm^3 and 2.0 g/cm^3 whereas, that of Li and Mg are negative for lower and higher densities. This is because Na atom has a higher ionic radius of 1.02 Å making it weakly bind with the structural carbon model framework at higher density compared to 0.76 Å and 0.72 Å for Li and Mg respectively. This implies that Na intercalation is thermodynamically more stable at low-density porous carbon than at higher density. The adsorption process can be divided into two stages, Na bonding with the disorder surfaces of carbons framework, and the atom condensation and metal formation.

Our results fit well with the experimental lithiation or sodiation voltage profiles of the porous hard carbons. The calculated adsorption reveals that the clustering of adatoms can exist in the pores as long as the discharge potential is low enough. Our estimate of the voltage is higher than the experimental values because the solid electrolyte interphase (SEI) which forms between the carbon anode and electrolytes during actual charging and discharging cycles were not considered in our simulations. Lastly, it is shown that the defected surface ratio plays a key role in the specific Li or Na storage capacity of the porous carbon materials. Therefore, by enlarging the area of the defected surface and the size of the holes, the Li or Na storage capacity in the anodic pores can be increased. To design or synthesis, an anode material for Na ion batteries the density of carbon is very important as lower densities provide more void and defected surfaces hence more sodium ion

absorption. Our analysis will help to better understand the Li or Na storage in the porous carbon materials and design Li- and Na-storage carbonaceous materials for the Na-ion batteries.

5.1 REFERENCES

(1). Valladares, A.A. A new approach to the ab initio generation of amorphous semiconducting structures. Electronic and vibrational studies. In Glass Materials Research Progress; Wolf, J.C.,Materials 2010, 3 500 Lange, L., Eds.; Nova Science Publishers, Inc.: New York, NY, USA, 2008; Chapter 3, pp. 61–123.

(2). Valladares, A.A.; Valladares, A.; Valladares, R.M. Mater. Res. Soc. Symp. Proc. 2007, 988, 97–102.

(3). I.shizaki, K.; Komarneni, S.; Nanko, M. Porous Materials. Process Technology and Applications, 1st ed., Materials Technology Series; Kluwer Academic Publishers: Boston, MA, USA, 1998; pp. 181–201.

(4). Smith, M.A.; Lobo, R.F. Microporous Mesoporous Mater. 2006, 92, 81–93.

(5). Petkov, V.; Difrancesco, R.G.; Billinge, S.J.L.; Acharya, M.; Foley, H.C. Local structure of nanoporous carbons. Phil. Mag. B 1999, 79, 1519–1530.

(6). Huheey, J.E.; Keiter, E.A.; Keiter, R.L. Inorganic Chemistry. Principles of Structure and Reactivity, 4th ed.; HarperCollins College Publishers: New York, NY, USA, 1993, pp. A-25, A-30.

(7). J.-M. Tarascon, Nature Chemistry 2 (2010) 510.

(8). M.D. Slater, D. Kim, E. Lee, C.S. Johnson, Adv. Funct. Mater. 23 (2013) 947-958.

(9). C. Grosjean, P.H. Miranda, M. Perrin, P. Poggi, 16 (2012) 1735-1744.

(10). P. Ge, M. Fouletier, , Solid State Ionics 28-30 (1988) 1172-1175.

(11). S. Komaba, Y. Matsuura, T. Ishikawa, N. Yabuuchi, W. Murata, S. Kuze, Electrochem. Commun. 21 (2012) 65-68.

(12). N. Yabuuchi, K. Kubota, M. Dahbi and S. Komaba, Chem. Rev., 2014, 114, 11636–11682.

(13). X. Xie, Z. Ao, D. Su, J. Zhang and G. Wang, Adv. Funct. Mater., 2015, 25, 1393–1403.

(14). J. K. Kim, Y. Kim, S. Park, H. Ko and Y. Kim, Energy Environ. Sci., 2016, 9, 1264–1269.

(15). Y. Fang, X.-Y. Yu and X. W. Lou, Angew. Chem., Int. Ed., 2017, 56, 5801–5805.

(16). D. A. S. a. J. R. Dahn, J. Electrochem. Soc., 2000, 147, 1271–1273.

(17). Y. Cao, L. Xiao, M. L. Sushko, W. Wang, B. Schwenzer, J. Xiao, Z. Nie, L. V. Saraf, Z. Yang and J. Liu, Nano Lett., 2012, 12, 3783–3787.

(18). B. Qu, C. Ma, G. Ji, C. Xu, J. Xu, Y. S. Meng, T. Wang and J. Y. Lee, Adv. Mater., 2014, 26, 3854–3859.

(19). F. Shen, W. Luo, J. Dai, Y. Yao, M. Zhu, E. Hitz, Y. Tang, Y. Chen, V. L. Sprenkle, X. Li and L. Hu, Adv. Energy Mater., 2016, 6, 1600377–1600383.

(20). K. Wang, Y. Xu, Y. Li, V. Dravid, J. Wu and Y. Huang, J. Mater. Chem. A, 2019, 7, 3327–3335.

(21). C. Matei Ghimbeu, J. G´orka, V. Simone, L. Simonin, S. Martinet and C. Vix-Guterl, Nano Energy, 2018, 44, 327–335.
(22). M. Dahbi, M. Kiso, K. Kubota, T. Horiba, T. Cha□k, K. Hida,T. Matsuyama and S. Komaba, J. Mter. Chem. A, 2017, 5,9917–9928.
(23). D. A. Stevens and J. R. Dahn, J. Electrochem. Soc., 2001, 148, A803–A811.
(24). Y. Qiao, X. Cheng, Y. Liu, R. Han, M. Ma, Q. Li, H. Dong, X. Li and S. Yang, Inorg. Chem. Front., 2017, 4, 2017–2023.
(25). Y. Liu, G. Wei, L. Pan, M. Xiong, H. Yan, Y. Li, C. Lu and Y. Qiao, ChemElectroChem, 2017, 4, 3244–3249.
(26). J. Yang, X. Zhou, D. Wu, X. Zhao and Z. Zhou, Adv. Mater., 2017, 29, 1604108–1604112.
(27). J. Qian, F. Wu, Y. Ye, M. Zhang, Y. Huang, Y. Xing, W. Qu, L. Li and R. Chen, Adv. Energy Mter., 2018, 8, 1703159.
(28). P. Lu, Y. Sun, H. Xiang, X. Liang and Y. Yu, Adv. Energy Mater., 2018, 8, 1702434–1702441.
(29). S. Wenzel, T. Hara, J. Janek and P. Adelhelm, Energy Environ. Sci., 2011, 4, 3342–3345.
(30). M. S. Islam and C. A. J. Fisher, Chem. Soc. Rev.,2014, 43, 185–204.
(31). A. Urban, D. Seo and G. Ceder, Comput. Mater., 2016, 2, 16002.
(32). A. Jain, Y. Shin and K. A. Persson, Nat. Rev. Mater., 2016, 1, 1–13.
(33). K. R. Kganyago and P. E. Ngoepe, Phys. Rev. B: Condens. Matter Mater. Phys., 2003, 68, 205111.
(34). K. Toyoura, Y. Koyama, A. Kuwabara, F. Oba and I. Tanaka, Phys. Rev. B: Condens. Matter Mater. Phys., 2008, 78, 214303.
(35). K. Persson, Y. Hinuma, Y. S. Meng, A. Van Der Ven and G. Ceder, Phys. Rev. B: Condens. Matter Mater. Phys., 2010, 82, 125416.
(36). V. Pande and V. Viswanathan, Phys. Rev. Mater., 2018, 2, 125401.
(37). E. Ziambaras, J. Kleis, E. Schr¨oder and P. Hyldgaard, Phys. Rev. B: Condens. Matter Mater. Phys., 2007, 76, 155425.
(38). W. Luo, J. Wan, B. Ozdemir, W. Bao, Y. Chen, J. Dai, H. Lin, Y. Xu, F. Gu, V. Barone and L. Hu, Nano Lett., 2015, 15, 7671–7677.
(39). Z. Xu, X. Lv, J. Chen, L. Jiang, Y. Lai and J. Li, Carbon, 2016, 107, 885–894.
(40). J. Liu, T. Yin, B. Tian, B. Zhang, C. Qian, Z. Wang, L. Zhang, P. Liang, Z. Chen, J. Yan, X. Fan, J. Lin, X. Chen, Y. Huang, K. P. Loh and Z. X. Shen, Adv. Energy Mater., 2019, 9, 1900579.
(41). P.-c. Tsai, S.-C. Chung, S.-k. Lin and A. Yamada, J. Mater. Chem. A, 2015, 3, 9763–9768.
(42). Z. Jian, C. Bommier, L. Luo, Z. Li, W. Wang, C. Wang, P. A. Greaney and X. Ji, Chem. Mater., 2017, 29, 2314–2320.
(43). C. Bommier, X. Ji and P. A. Greaney, Chem. Mater., 2019, 31, 658–677.
(44). F. Legrain, J. Sottmann, K. Kotsis, S. Gorantla, S. Sartori and S. Manzhos, J. Phys. Chem. C, 2015, 119, 13496–13501.
(45). M. K. Y. Chan, C. Wolverton and P. Greeley, J. Am. Chem.Soc., 2012, 134, 14362–14374.
(46). R. C. Powles, N. A. Marks and D. W. M. Lau, Phys. Rev. B: Condens. Matter Mater. Phys., 2009, 79, 075430.
(47). J. C. Palmer, A. Llobet, S.-H. Yeon, J. E. Fischer, Y. Shi, Y. Gogotsi and K. E. Gubbins, Carbon, 2010, 48, 1116–1123.
(48). S. Schweizer, R. Meissner, M. Amkreutz, K. Thiel, P. Schiffels, J. Landwehr, B. J. M. Etzold and J.-R. Hill, J. Phys. Chem. C, 2017, 121, 7221–7231.

(49). L. M. Mej´ıa-Mendoza, M. Valdez-Gonzalez, J. Mu˜niz, U. Santiago, A. K. Cuentas-Gallegos and M. Robles, Carbon, 2017, 120, 233–243.
(50). R. Ranganathan, S. Rokkam, T. Desai and P. Keblinski, Carbon, 2017, 113, 87–99.
(51). M. Raju, P. Ganesh, P. R. C. Kent and A. C. T. van Duin, , J. Chem. Theory Comput., 2015, 11, 2156–2166.
(52). E. Hjertenaes, A. Q. Nguyen and H. Koch, Phys. Chem. Chem. Phys., 2016, 18, 31431–31440.
(53). Fleur Legrain, , J. Phys. Chem. C 2015, 119, 13496−13501.
(54). Jian-Xing Huang, G´abor Cs´anyi,b Jin-Bao Zhao, J. Mater. Chem. A, 2019, 7, 19070–19080.
(55). Junyu Jiao, Ruijuan Xiao, Meng Tian. Electrochimica Acta 282 (2018) 205, 212.